nature sustainability

Article

https://doi.org/10.1038/s41893-022-00993-7

Atomically dispersed bimetallic Fe–Co electrocatalysts for green production of ammonia

In the format provided by the authors and unedited

Supplementary information for

Controllable synthesis of atomically-dispersed bimetallic electrocatalysts for green production of ammonia

Shengbo Zhang[1,2,8], Miaomiao Han[3,8], Tongfei Shi[1,2,8], Haimin Zhang[1,2*], Yue Lin[4], Xusheng Zheng[5], Li Rong Zheng[6], Hongjian Zhou[1,2], Chun Chen[1,2], Yunxia Zhang[1,2], Guozhong Wang[1,2], Huajie Yin[1,2], Huijun Zhao[7*]

[1] Key Laboratory of Materials Physics, Centre for Environmental and Energy Nanomaterials, Anhui Key Laboratory of Nanomaterials and Nanotechnology, CAS Center for Excellence in Nanoscience, Institute of Solid State Physics, HFIPS, Chinese Academy of Sciences, Hefei 230031, China.

[2] University of Science and Technology of China, Hefei 230026, China.

[3] School of Science, Huzhou University, Huzhou, Zhejiang 313000, China.

[4] Hefei National Research Center for Physical Sciences at the Microscale, University of Science and Technology of China, Hefei 230026, China.

[5] National Synchrotron Radiation Laboratory, University of Science and Technology of China, Hefei 230029, China.

[6] Beijing Synchrotron Radiation Facility, Institute of High Energy Physics, Chinese Academy of Sciences, 19B Yuquan Road, Beijing 100049, China.

[7] Centre for Catalysis and Clean Energy, Griffith University, Gold Coast Campus, QLD 4222, Australia.

[8] These authors contributed equally: Shengbo Zhang, Miaomiao Han, Tongfei Shi.

*Correspondence: h.zhao@griffith.edu.au (H.Z.), zhanghm@issp.ac.cn (H.Z.).

Supplementary Table 1. NRR performance of the reported NRR electrocatalysts and Fe/Co-O-C-1.0.

References	Catalyst	Conditions	NH_3 Production Rate	Faradaic Efficiency (%)	Detection method
		Noble Metal Electrocatalysts			
1	Pd nanoparticles	0.1 M PBS	4.2 μg h^{-1} $mg_{cat.}^{-1}$ (0.1 V *vs.* RHE)	8.2	Indophenol method
2	Au/TiO_2	0.1 M HCl	21.4 μg h^{-1} $mg_{cat.}^{-1}$ (−0.2 V *vs.* RHE)	8.11	Indophenol method
3	$Pd_{0.2}/Cu_{0.8}$ nanoclusters	0.1 M KOH	1.66 μg h^{-1} $mg_{cat.}^{-1}$ (−0.2 V *vs.* RHE)	4.52	Indophenol method
4	Ag nanosheets	0.1 M HCl	2.8 μg h^{-1} cm^{-2} (−0.6 V *vs.* RHE)	4.8	Indophenol method
5	Ag-Au@ZIF	$LiCF_3SO_3$ 1% EtOH in THF	10 pmol cm^{-2} s^{-1} (−2.9 V *vs.* Ag/AgCl)	18 ± 4	Indophenol method
6	Au_6/Ni	0.05 M H_2SO_4	7.4 μg h^{-1} $mg_{cat.}^{-1}$ (−0.14 V *vs.* RHE)	67.8	Indophenol method
7	Rh-Se NCs	0.1 M HCl	175.6 ± 23.6 μg h^{-1} $mg_{cat.}^{-1}$ (−0.1 V *vs.* RHE)	13.3 ± 0.4	Indophenol method
8	np-$PdH_{0.43}$	0.1 M PBS	20.4 μg h^{-1} $mg_{cat.}^{-1}$ (−0.15 V *vs.* RHE)	43.6	Indophenol method
9	Ru/rGO	0.05 M H_2SO_4	50 μg h^{-1} $mg_{cat.}^{-1}$ (−0.1 V *vs.* RHE)	11	Indophenol method
10	Au_{25}-Cys-Mo	0.1 M HCl	34.5 μg h^{-1} $mg_{cat.}^{-1}$ (−0.2 V *vs.* RHE)	26.5	Indophenol method
11	Pd/HsGDY	0.05 M H_2SO_4	115.93 μg h^{-1} $mg_{cat.}^{-1}$ (−0.25 V *vs.* RHE)	44.45	Indophenol method
		Metal Free Electrocatalysts			
12	NPC-500	0.005 M H_2SO_4	22.3 μg h^{-1} $mg_{cat.}^{-1}$ (−0.4 V *vs.* RHE)	9.58	Indophenol method
13	B_4C nanosheet	0.1 M HCl	26.57 μg h^{-1} $mg_{cat.}^{-1}$ (−0.75 V *vs.* RHE)	15.95	Indophenol method
14	Fluorine-doped carbon	0.05 M H_2SO_4	6.9 μg h^{-1} cm^{-2} (−0.55 V *vs.* RHE)	12.1	Indophenol method
15	Boron phosphide	0.1 M HCl	26.24 μg h^{-1} $mg_{cat.}^{-1}$ (−0.6 V *vs.* RHE)	12.7	Indophenol method

16	BNS/CP	0.1 M Na_2SO_4	13.22 μg h^{-1} $mg_{cat.}^{-1}$ (−0.8 V *vs.* RHE)	4.04	Indophenol method
17	Eex-COF/NC	0.1 M KOH	12.53 μg h^{-1} $mg_{cat.}^{-1}$ (−0.2 V *vs.* RHE)	45.43	Indophenol method
18	Molten LiCl-KCl	LiCl-KCl	2.4×10^{-8} mol cm^{-2} s^{-1} (0.7 V *vs.* Li^+/Li)	4.2	NH_3 ISE
19	F-doped carbon	0.05 M H_2SO_4	197.7 μg h^{-1} $mg_{cat.}^{-1}$ (−0.3 V *vs.* RHE)	54.8 (−0.2 V *vs.* RHE)	Indophenol method
20	BND_2-NC/Ti	0.05 M H_2SO_4 + 0.2 M $LiSO_4$	19.1 μg h^{-1} cm^{-2} (−0.7 V *vs.* RHE)	21.2	Indophenol method
21	cRP NRs	0.1 M Na_2SO_4	15.4 μg h^{-1} $mg_{cat.}^{-1}$ (−0.4 V *vs.* RHE)	9.4 (−0.2 V *vs.* RHE)	Indophenol method
			Transition Metal Electrocatalysts		
22	Cu/PI-300	0.1 M KOH	12.4 μg cm^{-2} h^{-1} (−0.3 V *vs.* RHE)	6.56	Indophenol method
23	Fe–Ni@C	0.1 M Na_2SO_4	1.72×10^{-10} mol cm^{-2} s^{-1} (−0.5 V *vs.* RHE)	23	Indophenol method
24	FeS_2-$Mo_{17.3}$	0.1 M KOH	25.15 μg h^{-1} $mg_{cat.}^{-1}$ (−0.2 V *vs.* RHE)	14.41	Indophenol method
25	GDY/Co_2N	0.1 M Na_2SO_4	219.72 μg h^{-1} $mg_{cat.}^{-1}$ (0.055 V *vs.* RHE)	58.60	Indophenol method
26	Fe-doped $W_{18}O_{49}$	0.25 M $LiClO_4$	24.7 μg h^{-1} $mg_{cat.}^{-1}$ (−0.15 V *vs.* RHE)	20.0	Indophenol method
27	Fe-ReS_2@N-CNF	0.1 M Na_2SO_4	80.4 μg h^{-1} $mg_{cat.}^{-1}$ (−0.2 V *vs.* RHE)	12.3	Indophenol method
28	Co_{SC}-N-C	0.1 M KOH	76.2 μg h^{-1} $mg_{cat.}^{-1}$ (−0.2 V *vs.* RHE)	52.9	Indophenol method
29	Mo_2C	0.1 M Na_2SO_4	3.36 μg cm^{-2} h^{-1} (−0.55 V *vs.* RHE)	40.2	Indophenol method
30	MoS_2/NC-900	0.1 M Na_2SO_4	36.1 μg h^{-1} $mg_{cat.}^{-1}$ (−0.50 V *vs.* RHE)	15.2	Indophenol method
31	$FeWS_x$@$FeWO_4$	1 M KOH	30.2 μg h^{-1} $mg_{cat.}^{-1}$ (−0.45 V *vs.* RHE)	16.4	Indophenol method
32	PAL-MoS_2	0.1 M HCl	3405.55 μg h^{-1} $mg_{cat.}^{-1}$ (−0.1 V *vs.* RHE)	44.36	Indophenol method

33	Mo-PTA@CNT	0.1 M K_2SO_4	51 ± 1 μg h^{-1} $mg_{cat.}^{-1}$ (−0.1 V *vs.* RHE)	83 ± 1	Indophenol method
			Main Group Metal Electrocatalysts		
34	PC/Sb/$SbPO_4$	0.1 M HCl	25 μg h^{-1} $mg_{cat.}^{-1}$ (−0.25 V *vs.* RHE)	31 (−0.15 V *vs.* RHE)	Indophenol method
35	BP@SnO_{2-x} nanotube	0.1 M Na_2SO_4	48.87 μg h^{-1} $mg_{cat.}^{-1}$ (−0.4 V *vs.* RHE)	14.6	Indophenol method
36	Bi NS	0.1 M Na_2SO_4	12.23 μg h^{-1} $mg_{cat.}^{-1}$ (−0.8 V *vs.* RHE)	10.46 ± 1.45	Indophenol method
37	BiNCs	0.5 M K_2SO_4	200 mmol g^{-1} h^{-1} (−0.6 V *vs.* RHE)	66	Nessler's reagent
38	R-O-Bi	0.2 M Na_2SO_4	5.453 μg h^{-1} mg_{Bi}^{-1} (−0.6 V *vs.* RHE)	11.68	Indophenol method
39	Bi NS/CF	0.1 M HCl	6.89×10^{-11} mol cm^{-2} s^{-1} (−0.5 V *vs.* RHE)	10.26	Indophenol method
40	Al-N_2 battery	0.05 M H_2SO_4	13.4 μg h^{-1} $mg_{cat.}^{-1}$ (−0.1 V *vs.* RHE)	5	Indophenol method
41	Bi NPs	0.1 M Na_2SO_4	3.25 ± 0.08 μg cm^{-2} h^{-1} (−0.7 V *vs.* RHE)	12.11 ± 0.84 (−0.6 V *vs.* RHE)	Indophenol method
42	Bi@C-900	0.1 M Na_2SO_4	4.22 ± 0.33 μg h^{-1} $mg_{cat.}^{-1}$ (−0.6 V *vs.* RHE)	15.10 ± 0.43 (−0.4 V *vs.* RHE)	Indophenol method
			Single-Atom Electrocatalysts		
43	Au SAs/C_3N_4 (Au-N bond)	0.005 M H_2SO_4	1305 μg h^{-1} mg_{Au}^{-1} (−0.2 V *vs.* RHE)	11.1	Indophenol method
44	Ru SAs/N-C (Ru-N bond)	0.05 M H_2SO_4	120.9 μg h^{-1} $mg_{cat.}^{-1}$ (−0.2 V vs. RHE)	29.6	Indophenol method
45	Ru@ZrO_2/NC (Ru-N bond)	0.1 M HCl	3665 μg h^{-1} mg_{Ru}^{-1} (−0.21 V vs. RHE)	21	Indophenol method
46	SA-Mo/NPC (Mo-N bond)	0.1 M KOH	34.0 ± 3.6 μg h^{-1} $mg_{cat.}^{-1}$ (−0.3 V vs. RHE)	14.6 ± 1.6	Indophenol method
47	Fe_{SA}-N-C (Fe-N bond)	0.1 M KOH	7.48 μg h^{-1} $mg_{cat.}^{-1}$ (0 V vs. RHE)	56.55	Indophenol method

48	ISAS-Fe-N-C (Fe-N bond)	0.1 M PBS	62.9 ± 2.7 μg h^{-1} $mg_{cat.}^{-1}$ (−0.4 V vs. RHE)	18.6 ± 0.8	Indophenol method
49	Mo^0/GDY (Mo-C bond)	0.1 M Na_2SO_4	145.4 μg h^{-1} $mg_{cat.}^{-1}$ (−1.2 V *vs.* SCE)	21	Indophenol method
50	NC-Cu SA (Cu-N bond)	0.1 M KOH	53.3 μg h^{-1} $mg_{cat.}^{-1}$ (−0.35 V vs. RHE)	13.8	Indophenol method
		0.1 M HCl	49.3 μg h^{-1} $mg_{cat.}^{-1}$ (−0.3 V vs. RHE)	11.7	
51	Fe_1-N-C (Fe-N bond)	0.1 M HCl	1.56 × 10^{-11} mol cm^{-2} s^{-1} (−0.05 V *vs.* RHE)	4.51	Indophenol method
52	Co SA/NPC (Co-N bond)	0.05 M Na_2SO_4	0.86 μmol cm^{-2} h^{-1} (−0.2 V vs. RHE)	10.5	Indophenol method
53	Ru SAs/g-C_3N_4 (Ru-N bond)	0.5 M NaOH	23.0 μg h^{-1} $mg_{cat.}^{-1}$ (−0.05 V vs. RHE)	8.3	Indophenol method
54	Fe-SAs/LCC/GC (Fe-O bond)	0.1 M KOH	307.7 μg h^{-1} $mg_{cat.}^{-1}$ (−0.15 V *vs.* RHE)	51.0	Indophenol method
55	Co-SAs/NC-L (Co-N bond)	0.005 M H_2SO_4	16.9 μg h^{-1} $mg_{cat.}^{-1}$ (−0.25 V *vs.* RHE)	27.4 (−0.15 V *vs.* RHE)	Indophenol method
56	Fe-SnO_2 (Fe-O bond)	0.1 M HCl	82.7 μg h^{-1} $mg_{cat.}^{-1}$ (−0.3 V *vs.* RHE)	20.4	Indophenol method
57	SA Ru-Mo_2CT_x (Ru-C(O) bond)	0.5 M K_2SO_4	40.57 μg h^{-1} $mg_{cat.}^{-1}$ (−0.3 V *vs.* RHE)	25.77	Indophenol method
58	Fe-MoS_2 (Fe-S bond)	0.1 M KCl	97.5 ± 6 μg h^{-1} cm^{-2} (−0.2 V vs. RHE)	31.6 ± 2	Indophenol method
59	MoSAs-Mo_2C/ NCNTs (Mo-N/C bond)	0.005 M H_2SO_4	16.1 μg h^{-1} $mg_{cat.}^{-1}$ (−0.25 V vs. RHE)	7.1	Indophenol method
60	Fe-MoS_2 (Fe-S bond)	0.5 M K_2SO_4	8.63 μg h^{-1} $mg_{cat.}^{-1}$ (−0.3 V vs. RHE)	18.8	Indophenol method
61	SA-Ag/NC (Ag-N bond)	0.1 M HCl	270.9 μg h^{-1} $mg_{cat.}^{-1}$ (−0.65 V *vs.* RHE)	21.9 (−0.60 V *vs.* RHE)	Indophenol method
62	Pd-GDY (Pd-N bond)	0.1 M Na_2SO_4	4.45 ± 0.3 mg h^{-1} mg_{Pd}^{-1} (−0.16 V *vs.* RHE)	31.62 ± 1.06	Indophenol method

63	Mn-O_3N_1/PC (Mn-N/O bond)	0.1 M HCl	66.41 ± 4.05 μg h^{-1} $mg_{cat.}^{-1}$ (−0.35 V *vs.* RHE)	8.91 ± 0.82	Indophenol method
64	Ni-N_x-C (Ni-N bond)	0.1 M KOH	81 ± 3 μg h^{-1} cm^{-2} (−0.3 V *vs.* RHE)	12.4 ± 1.5	Indophenol method
65	Y_1/NC (Y-N/C bond)	0.1 M HCl	23.2 μg h^{-1} cm^{-2} (−0.1 V *vs.* RHE)	12.1	Indophenol method
	Sc_1/NC (Sc-N/C bond)		20.4 μg h^{-1} cm^{-2} (−0.1 V *vs.* RHE)	11.2	
	Dual-Atom Electrocatalysts				
66	CNT@C_3N_4-Fe&Cu (Fe-N and Cu-N bond)	0.001 M H_2SO_4	9.86 μg h^{-1} $mg_{cat.}^{-1}$ (−1.2 V vs. Ag/AgCl)	34.0 (−0.8 V vs. Ag/AgCl)	Indophenol method
67	PdCu/NC (Pd-Cu bond)	0.05 M H_2SO_4	69.2 ± 2.5 μg h^{-1} $mg_{cat.}^{-1}$ (−0.45 V *vs.* RHE)	24.8 ± 0.8	Indophenol method
This work	Fe/Co-O-C-1.0 (Fe-Co bond)	0.1 M Na_2SO_4	574.8 ± 35.3 μg h^{-1} $mg_{cat.}^{-1}$ (−0.30 V vs. RHE) (GC disk, Loading: 0.5 mg cm^{-2})	73.2 ± 4.6	Indophenol method
			577.2 ± 26.2 μg h^{-1} $mg_{cat.}^{-1}$ (−0.30 V vs. RHE) (GC plate, Loading: 0.5 mg cm^{-2})	70.6 ± 3.2	
			579.2 ± 27.8 μg h^{-1} $mg_{cat.}^{-1}$ (−0.30 V vs. RHE) (GC plate, Loading: 1.5 mg cm^{-2})	79.0 ± 3.8	

Supplementary Table 2. Impregnated Fe^{3+}/Co^{2+} contents on BC from different adsorption solutions and corresponding Fe/Co and Fe/Co SAs loaded on CBC.

$[Fe^{3+}]/[Co^{2+}]$ in Adsorption Solution (mmol L^{-1})	**Impregnated Fe^{3+}/Co^{2+} in Fe^{3+}-20-BC, Fe^{3+}/Co^{2+}-*x/y*-BC, Co^{2+}-20-BC†** (mmol g^{-1})	**Fe/Co in Fe-20-CBC, Fe/Co-*x/y*-CBC, Co-20-CBC†** (mmol g^{-1})	**Fe/Co SAs in Fe-O-C, Fe/Co-O-C-*r*, Co-O-C†** (wt.%)	**Fe/Co SAs in Fe-O-C, Fe/Co-O-C-*r*, Co-O-C†** (mmol g^{-1})	**Fe/Co Atomic Ratio in Fe/Co-O-C-*r***
20/-	0.54/-	1.65/-	0.27/-	0.0480/-	-
15/5.0	0.42/0.13	1.29/0.40	0.22/0.08	0.0391/0.0135	2.9
10/10	0.31/0.20	0.94/0.61	0.18/0.13	0.0320/0.0219	1.5
5.0/15	0.24/0.25	0.74/0.77	0.15/0.16	0.0266/0.0269	1.0
1.0/19	0.12/0.30	0.37/0.91	0.1/0.19	0.0178/0.0319	0.56
-/20	-/0.32	-/0.99	-/0.22	-/0.0370	-

†Determined by ICP-AES.

Supplementary Table 3. BET specific surface area and average pore volume of Fe-O-C, Co-O-C, Fe/Co-O-C-*r* and CBC.

Samples	BET Specific Surface Area (m^2 g^{-1})	Average Pore Diameter (nm)
Fe-O-C	559.2	0.84
Co-O-C	416.7	0.59
Fe/Co-O-C-2.9	463.5	0.70
Fe/Co-O-C-1.5	522.0	0.88
Fe/Co-O-C-1.0	490.0	0.71
Fe/Co-O-C-0.56	368.4	0.61
CBC	497.3	0.89

Supplementary Table 4. EXAFS fitting results of Fe/Co-O-C-1.0.

Sample	Edge	Scattering Pair	CN	R (Å)	σ^2 (10^{-3}Å^2)	ΔE_0 (eV)
As-synthesised Fe/Co-O-C-1.0	Fe	Fe-O	2.80	2.00	4.13	6.62
		Fe-Co	1.00	2.13	4.22	9.55
	Co	Co-O	2.80	2.05	6.63	−3.84
		Co-Fe	0.80	2.11	7.03	−8.12
Fe/Co-O-C-1.0 after10 NRR cycles	Fe	Fe-O	3.00	1.96	8.80	−7.79
		Fe-Co	1.00	2.10	6.29	2.47
	Co	Co-C	2.00	2.23	3.44	7.39
		Co-O	1.00	1.94	3.45	−8.62
		Co-Fe	1.00	2.07	6.19	0.12

CN: Coordination number; R: Interatomic distance (the bond length between central atoms and surrounding coordination atoms); σ^2: Debye-Waller factor (a measure of thermal and static disorder in absorber-scatter distances); ΔE_0: Edge-energy shift (the difference between the zero kinetic energy value of the sample and that of the theoretical model).

Supplementary Table 5. Loaded Fe, Co and bimetallic Fe-Co SAs on CBC.

Sample	Fe SAs† (μmol g^{-1})	Co SAs† (μmolg^{-1})	Total Fe/Co SAs† (μmol g^{-1})	Assumed Bimetallic Fe-Co Loading (μmol g^{-1})	Bimetallic Fe-Co Loading Density* (nmol cm^{-2})
Fe-O-C	47.95	-	-	-	-
Fe/Co-O-C-2.8	39.07	13.45	52.52	13.45	6.72
Fe/Co-O-C-1.5	31.96	21.85	53.81	21.85	10.93
Fe/Co-O-C-1.0	26.61	26.89	53.5	26.61	13.31
Fe/Co-O-C-0.56	17.75	31.93	49.68	17.75	8.87
Co-O-C	-	37.0	-	-	-

†Determined by ICP-AES.

*The bimetallic loading densities (D) were calculated according to:

D (nmol cm^{-2}) = m × ω

where, m is the catalyst loading on GC disk electrode (0.50 mg cm^{-2}), ω is the assumed bimetallic Fe-Co loadings (μmol g^{-1}).

Supplementary Table 6. Mass and geometric area activities, and FEs obtained from GC plate electrode (1.0 × 1.0 cm^{-2}) with different Fe/Co-O-C-1.0 loading densities.*

Catalyst Loading ($mg\ cm^{-2}$)	**Mass Activity** ($\mu g\ h^{-1}\ mg_{cat.}^{-1}$)	**Area Activity** ($nmol\ s^{-1}\ cm^{-2}$)	**Faradic Efficiency** (%)
0.50	577.2 ± 26.2	4.7 ± 0.2	70.6 ± 3.2
0.75	578.3 ± 26.6	7.1 ± 0.3	73.3 ± 3.4
1.0	578.8 ± 25.5	9.5 ± 0.4	76.2 ± 3.4
1.5	579.2 ± 27.8	14.2 ± 0.7	79.0 ± 3.8

*The presented data are obtained from three replicated experiments.

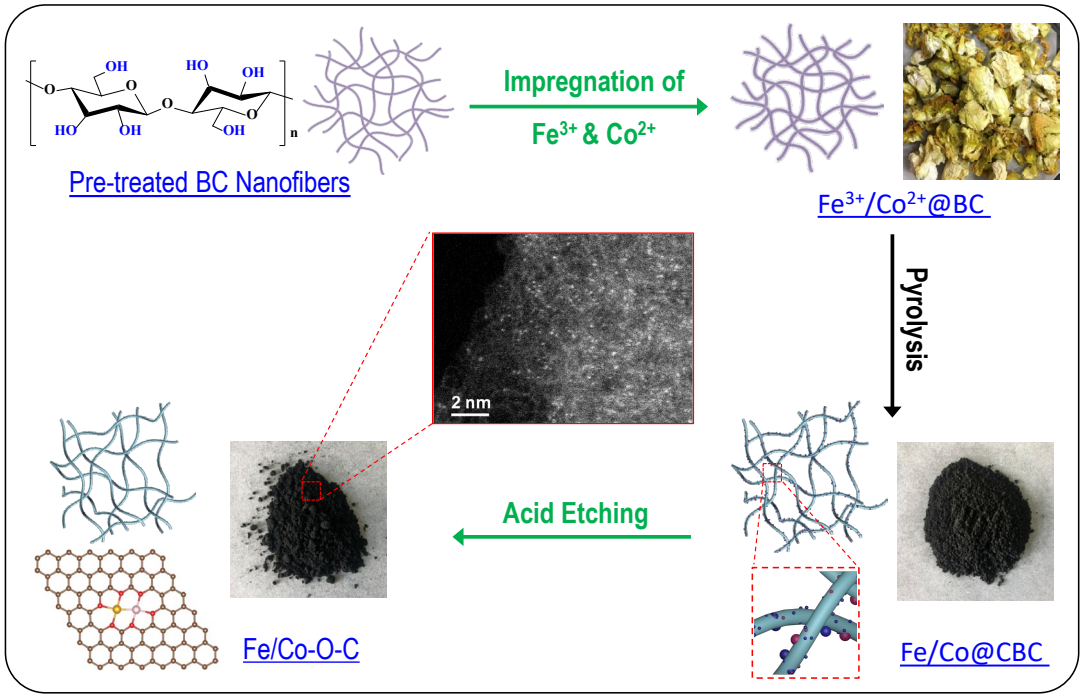

Supplementary Figure 1. Schematic diagram illustrating synthetic procedure of Fe/Co-O-C.

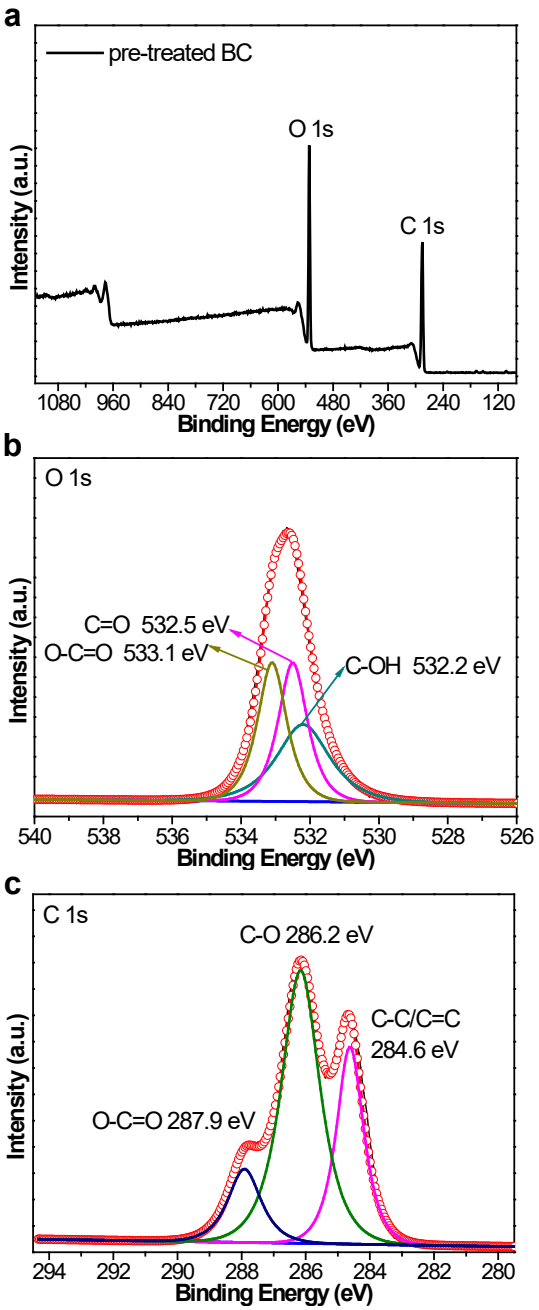

Supplementary Figure 2. (**a**) Surface survey XPS spectrum and high-resolution XPS spectra of (**b**) O *1s*, (**c**) C *1s* of pre-treated BC.

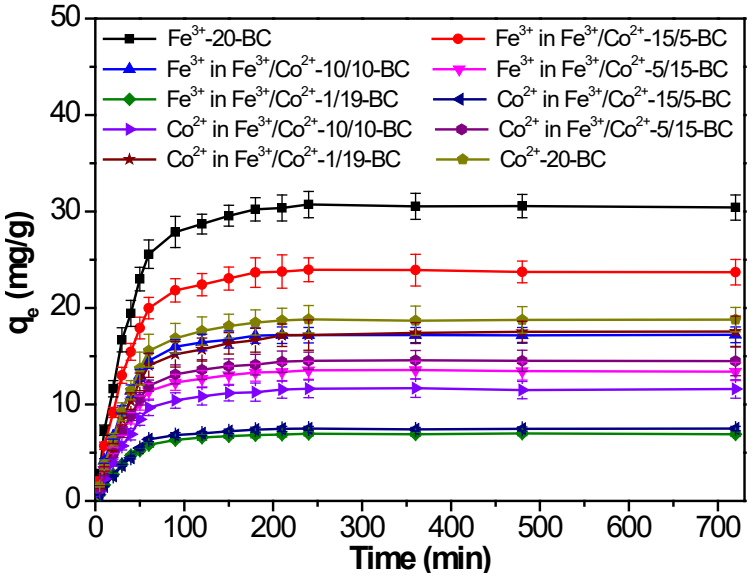

Supplementary Figure 3. Adsorption of Fe^{3+}, Co^{2+} and Fe^{3+}/Co^{2+}on BC at 25 °C. Adsorption solutions were prepared by dissolving appropriate amounts of $Co(SO_4)_3{\cdot}7H_2O$ and $Fe_2(SO_4)_3{\cdot}10H_2O$ in deionised water. The adsorption solutions for Fe^{3+}-20-BC and Co^{2+}-20-BC contain 20 mmol L^{-1} of Fe^{3+} or Co^{2+}, respectively. The adsorption solutions for Fe^{3+}/Co^{2+}-*x*/*y*-BC (*x*/*y*: $[Fe^{3+}]/[Co^{2+}]$ ratios in adsorption solutions) contain a total Fe^{3+} and Co^{2+} concentration of 20 mmol L^{-1} with different *x*/*y* values of 15/5, 10/10, 5/15 and 1/19. Adsorption solution volume: 400 mL; Amount of BC: 1.0 g; q_e: Impregnated Fe^{3+}/Co^{2+} amount on BC under equilibrium condition determined by ICP-AES.

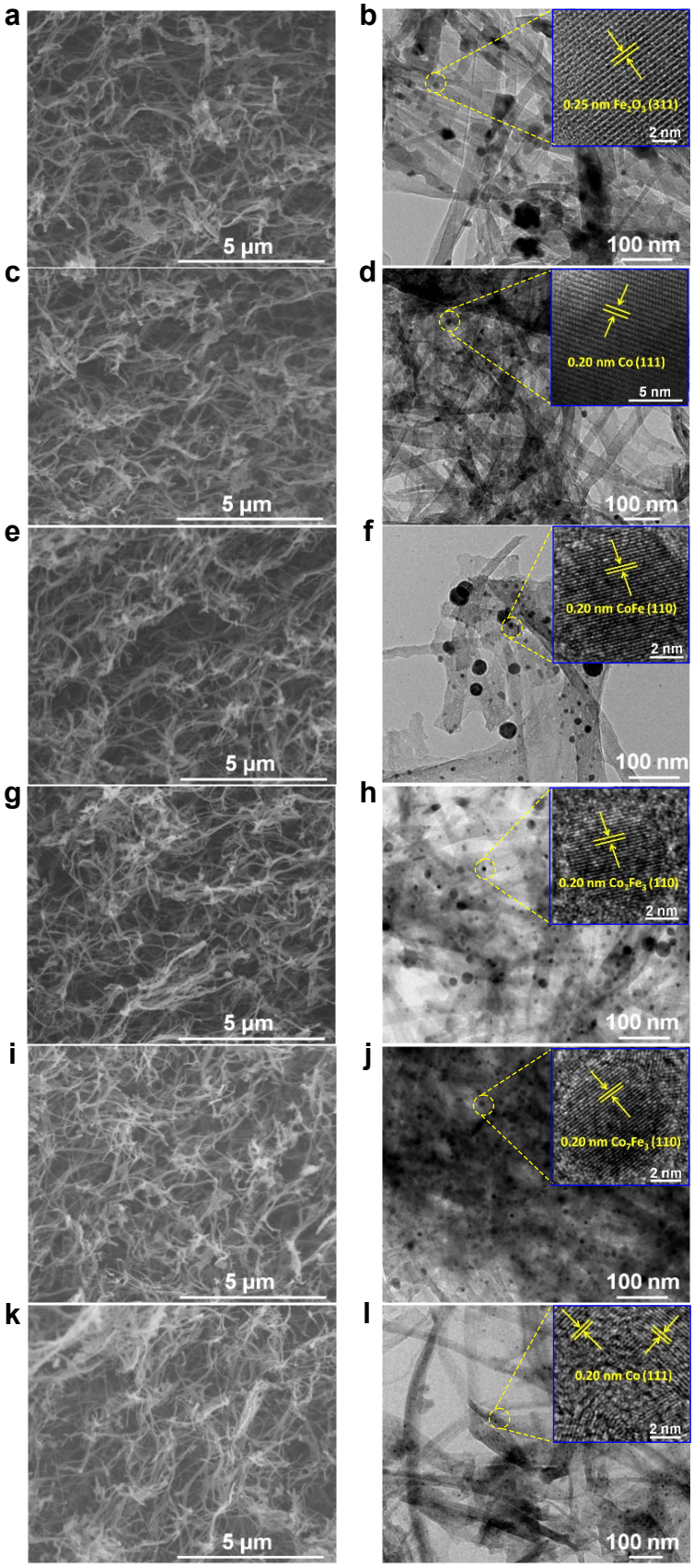

Supplementary Figure 4. SEM images and TEM images (Inset: HRTEM images) of (**a**, **b**) Fe-20-CBC, (**c**, **d**) Co-20-CBC, (**e**, **f**) Fe/Co-15/5-CBC, (**g**, **h**) Fe/Co-10/10-CBC, (**i**, **j**) Fe/Co-5/15-CBC and (**k**, **l**) Fe/Co-1/19-CBC.

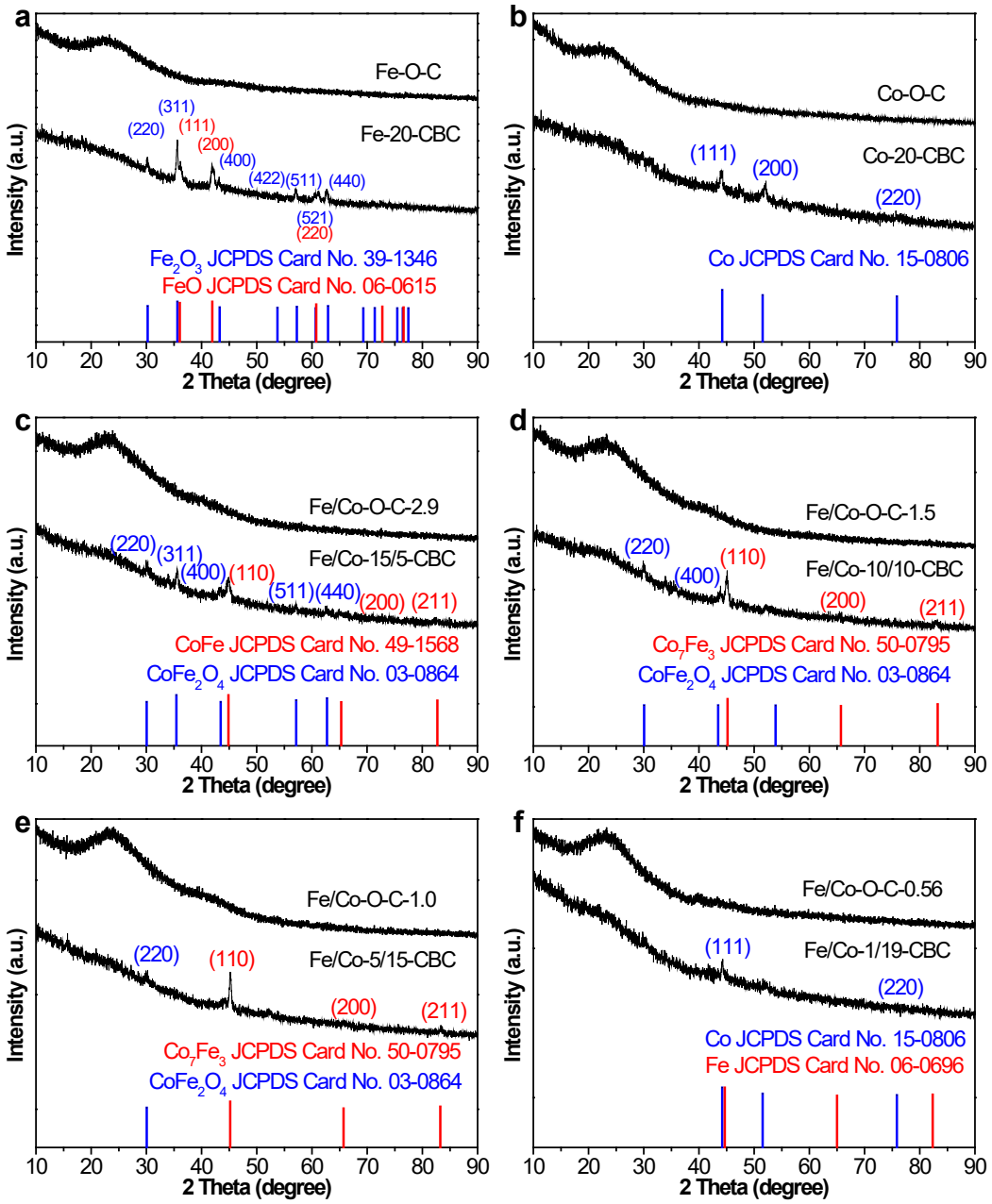

Supplementary Figure 5. XRD patterns of (**a**) Fe-20-CBC and Fe-O-C, (**b**) Co-20-CBC and Co-O-C, (**c**) Fe/Co-15/5-CBC and Fe/Co-O-C-2.9, (**d**) Fe/Co-10/10-CBC and Fe/Co-O-C-1.5, (**e**) Fe/Co-5/15-CBC and Fe/Co-O-C-1.0, (**f**) Fe/Co-1/19-CBC and Fe/Co-O-C-0.56.

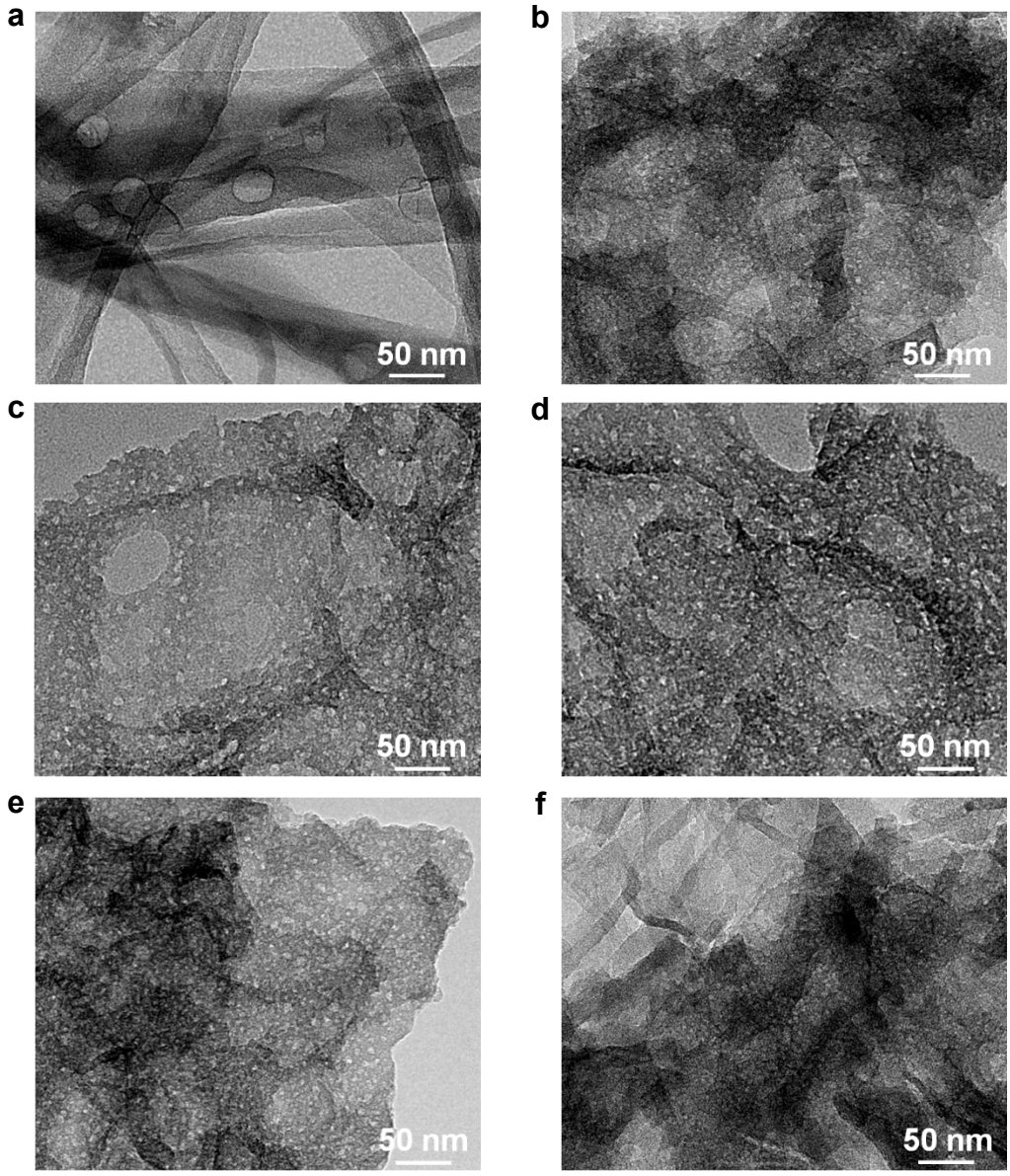

Supplementary Figure 6. TEM images of (**a**) Fe-O-C, (**b**) Co-O-C, (**c**) Co-O-C-2.9, (**d**) Fe/Co-O-C-1.5, (**e**) Fe/Co-O-C-1.0 and (**f**) Fe/Co-O-C-0.56 derived respectively from the acid-etched Fe-20-CBC, Co-20-CBC, Fe/Co-15/5-CBC, Fe/Co-10/10-CBC, Fe/Co-5/15-CBC and Fe/Co-1/19-CBC.

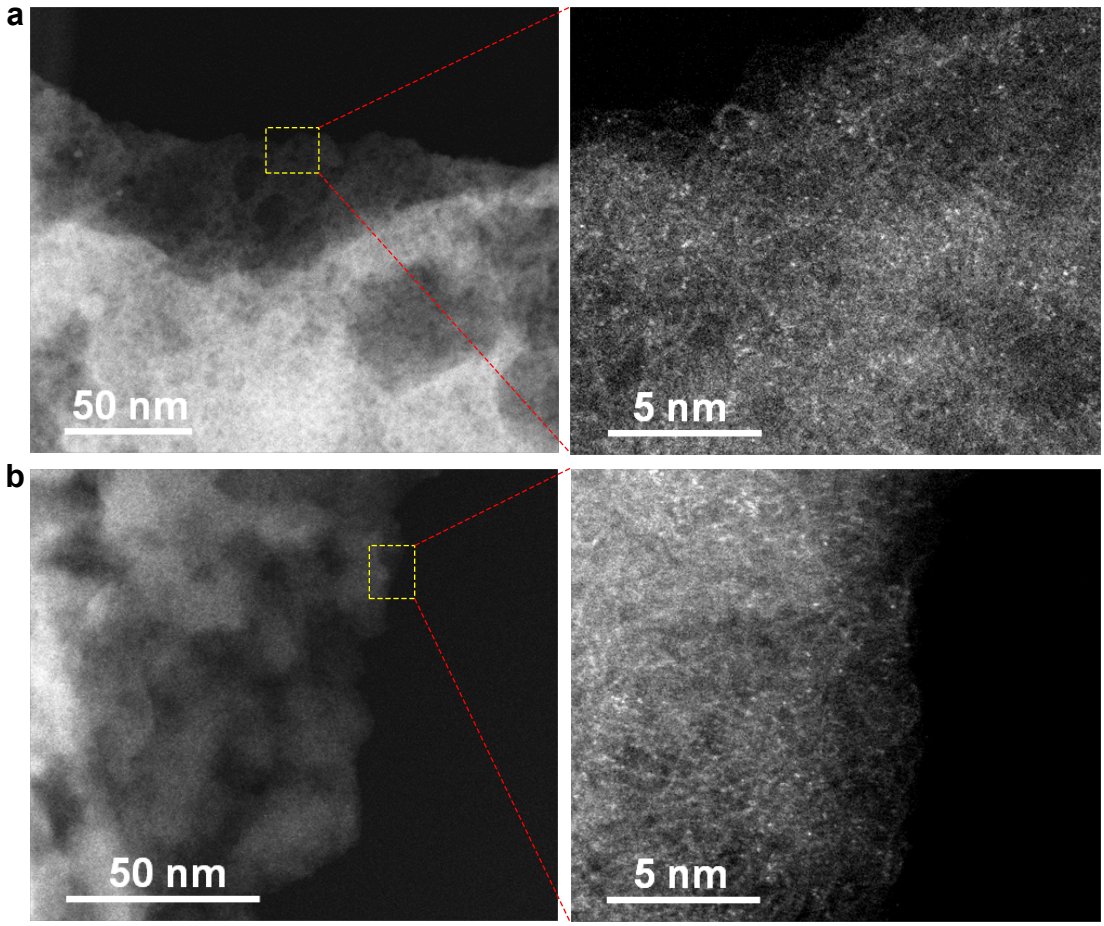

Supplementary Figure 7. HAADF-STEM images of (**a**) Fe-O-C and (**b**) Co-O-C derived respectively from the acid-etched Fe-20-CBC and Co-20-CBC.

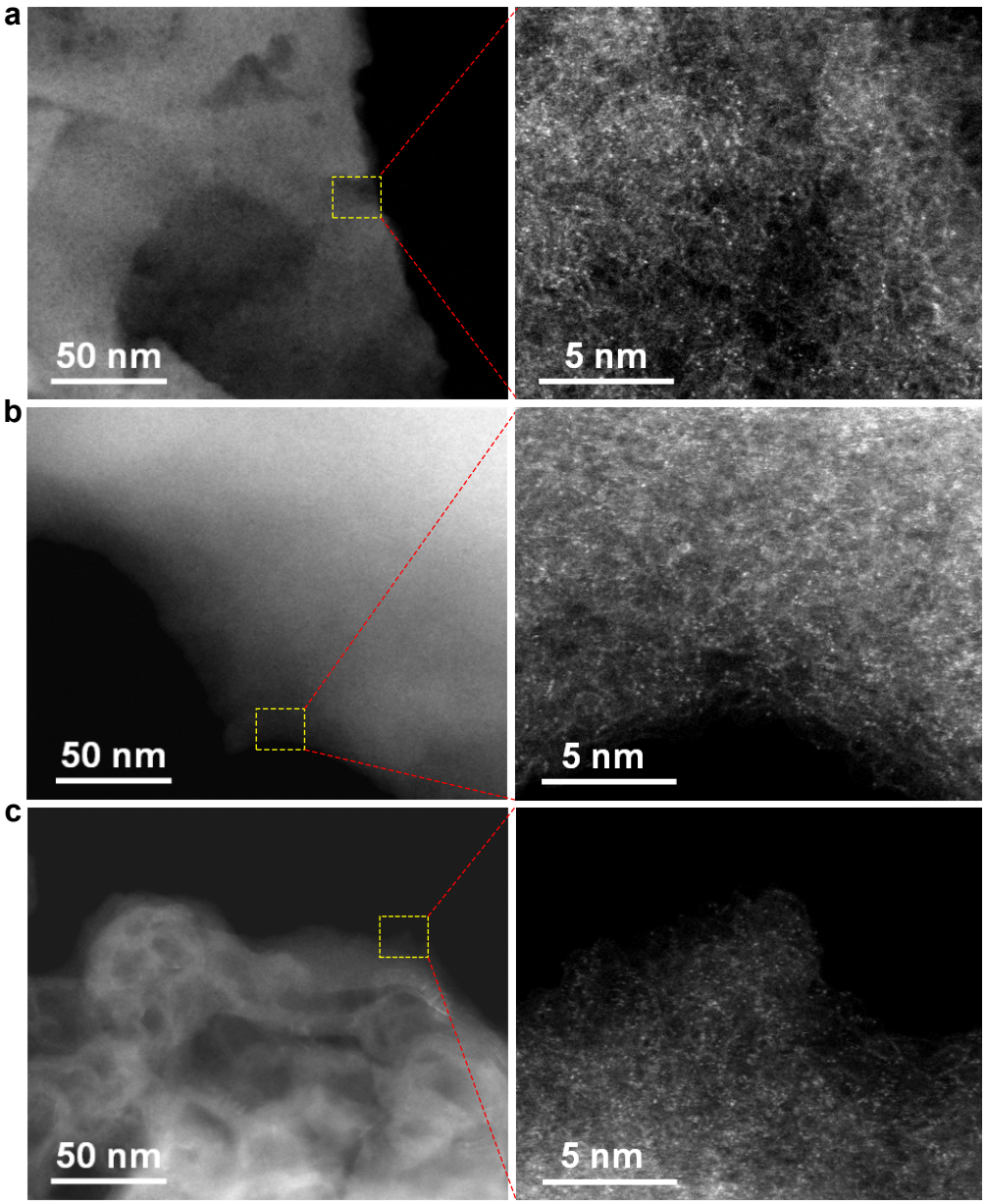

Supplementary Figure 8. HAADF-STEM images of (**a**) Fe/Co-O-C-0.56, (**b**) Fe/Co-O-C-1.5 and (**c**) Fe/Co-O-C-2.9 derived respectively from the acid-etched Fe/Co-1/19-CBC, Fe/Co-10/10-CBC and Fe/Co-15/5-CBC.

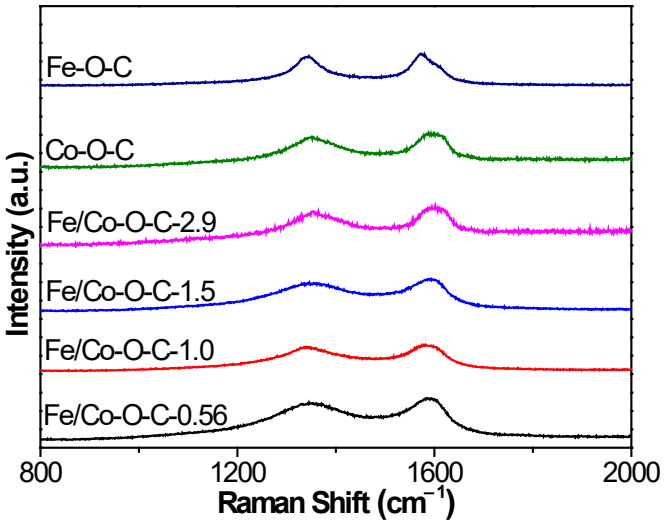

Supplementary Figure 9. Raman spectra of Fe-O-C, Co-O-C, Fe/Co-O-C-2.9, Fe/Co-O-C-1.5, Fe/Co-O-C-1.0 and Fe/Co-O-C-0.56.

The peaks at ~1346 and ~1588 cm^{-1} are assignable to the D and G bands of graphitic carbon, respectively.

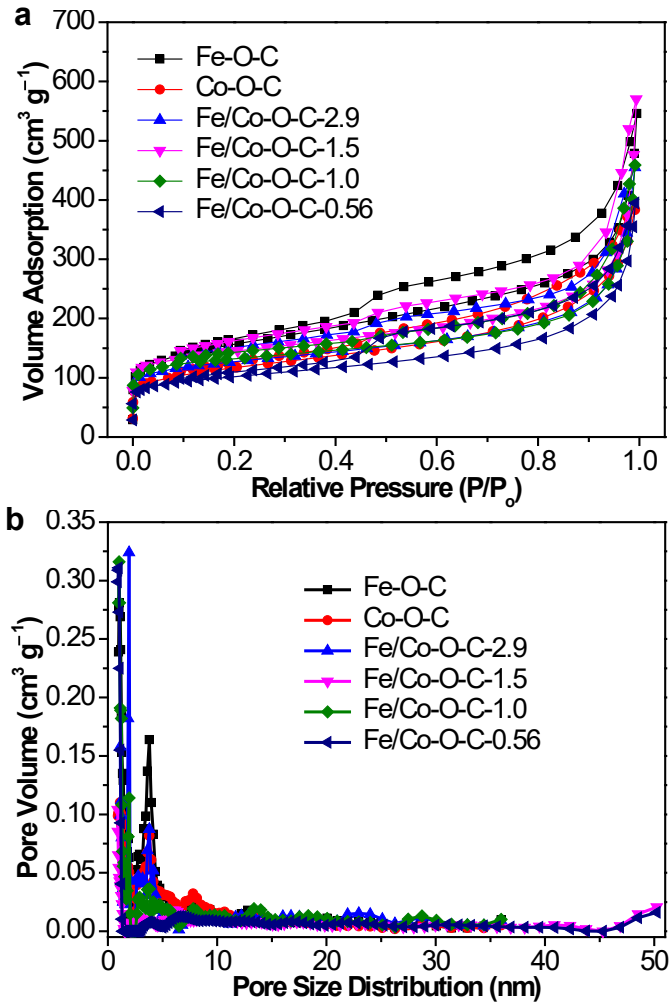

Supplementary Figure 10. (**a**) N_2 adsorption-desorption isotherms and (**b**) Corresponding pore size distribution curves of Fe-O-C, Co-O-C, Fe/Co-O-C-2.9, Fe/Co-O-C-1.5, Fe/Co-O-C-1.0 and Fe/Co-O-C-0.56.

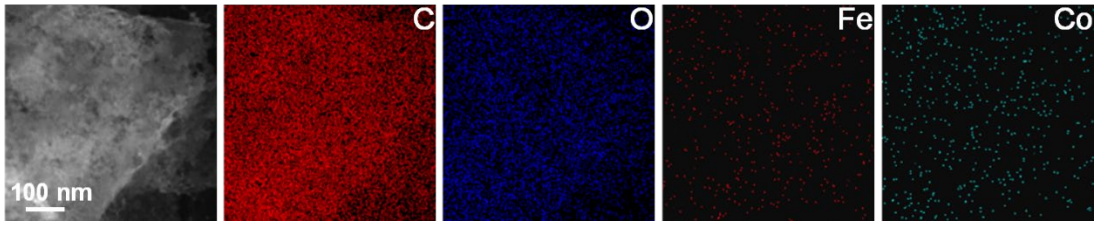

Supplementary Figure 11. HAADF-STEM image of Fe/Co-O-C-1.0 and corresponding elemental mapping images.

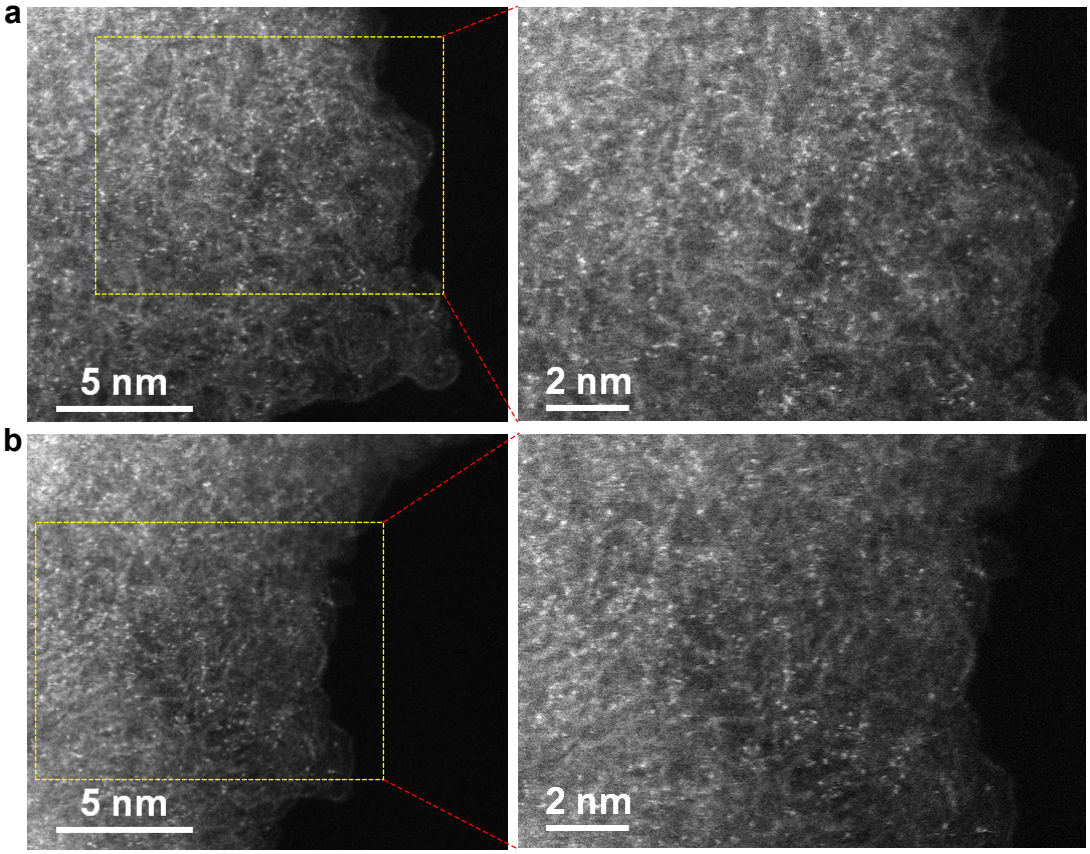

Supplementary Figure 12. HAADF-STEM images obtained from different locations of a Fe/Co-O-C-1.0 sample.

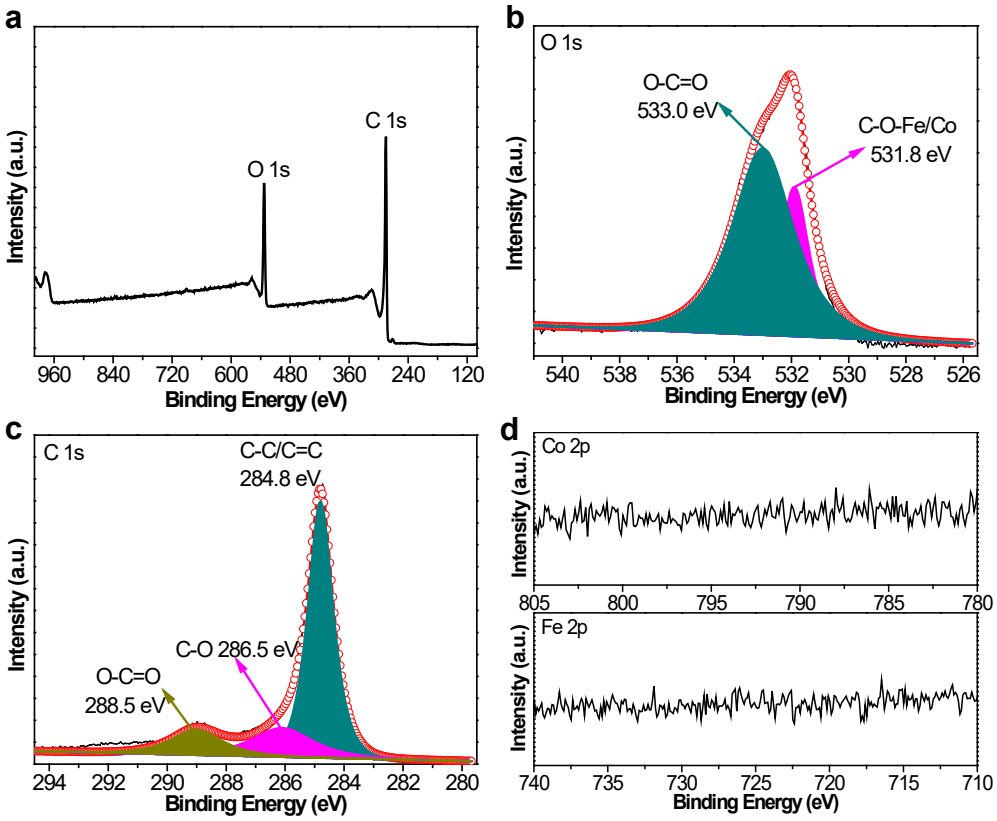

Supplementary Figure 13. (**a**) Survey XPS spectrum and high-resolution XPS spectra of (**b**) O *1s*, (**c**) C *1s* and (**d**) Co *2p* and Fe *2p* of Fe/Co-O-C-1.0.

The undetectable Fe/Co elements in Co 2*p* and Fe 2*p* XPS spectra (**d**) are due to the low Fe/Co contents[68].

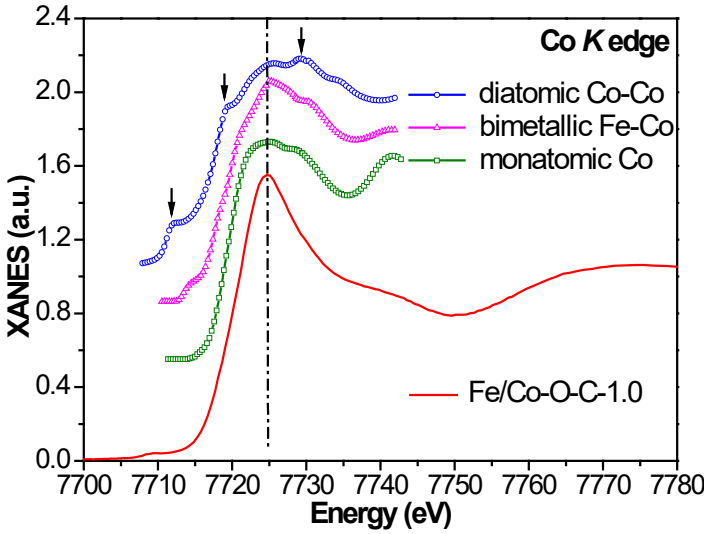

Supplementary Figure 14. Experimentally recorded Co *K* edge XANES spectrum of Fe/Co-O-C-1.0, and theoretically calculated XANES spectra of diatomic Co-Co, monatomic Co and bimetallic Fe-Co. Note that the XANES spectra were calculated by *FEFF*8.4 code.

We further calculated the XANES spectra for diatomic Co-Co, monatomic Co and bimetallic Fe-Co using *FEFF*8.4 code. It can be seen that experimentally recorded XANES spectrum from Fe/Co-O-C-1.0 sample show a characteristic peak at 7725 eV, which is coincided with the calculated XANES spectra of the bimetallic Fe-Co. In strong contrast, the calculated XANES spectrum for the diatomic Co-Co shows a strong peak at 7729 eV with two shoulder peaks at 7712 and 7719 eV, which differ marked from the experimentally measured XANES spectrum from Fe/Co-O-C-1.0. The above results can be used as additional evidence to support the presence of bimetallic Fe-Co sites in Fe/Co-O-C-1.0.

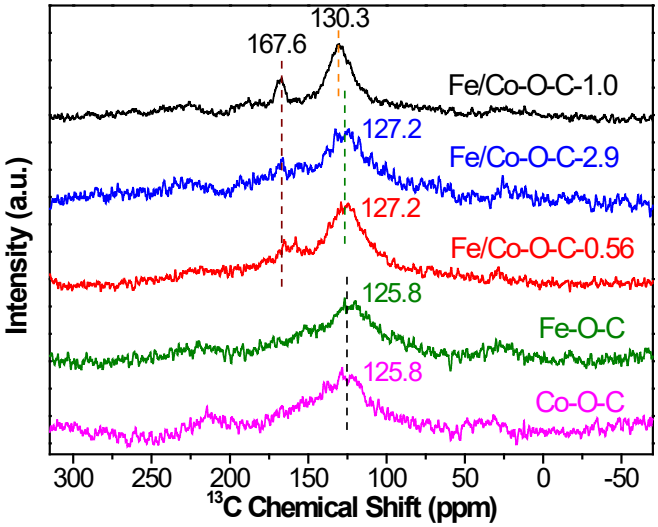

Supplementary Figure 15. Solid-state ^{13}C NMR spectra of Co-O-C, Fe-O-C, Fe/Co-O-C-0.56, Fe/Co-O-C-2.9 and Fe/Co-O-C-1.0.

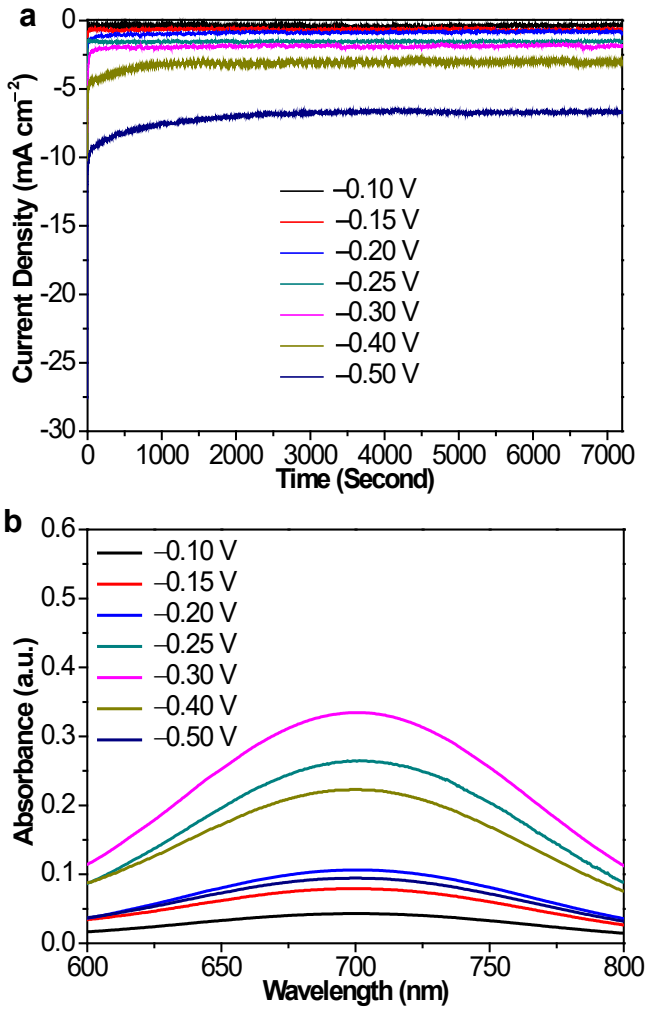

Supplementary Figure 16. (**a**) Time-dependent current density curves of Fe/Co-O-C-1.0 catalysed NRR at different potentials in N_2-saturated 0.1 M Na_2SO_4 electrolyte over a 2 h period. (**b**) UV-Vis absorption spectra of the corresponding samples recorded in accordance with the indophenol blue method.

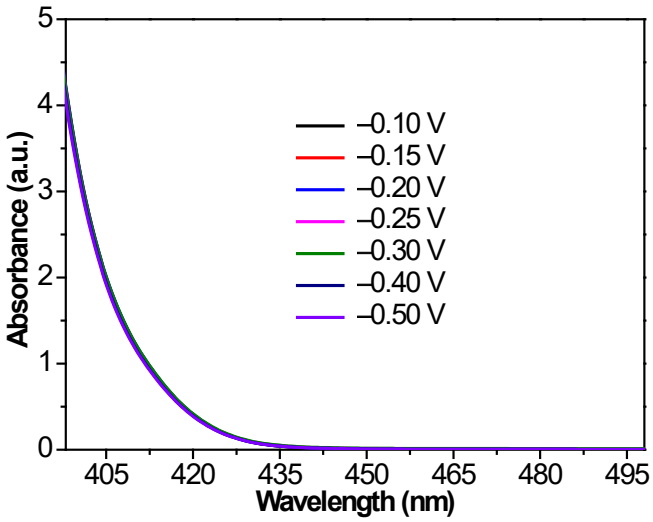

Supplementary Figure 17. UV-Vis absorption spectra of samples resulted from Fe/Co-O-C-1.0 catalysed NRR at different potentials in N_2-saturated 0.1 M Na_2SO_4 for 2 h recorded in accordance with Watt and Chrisp method.

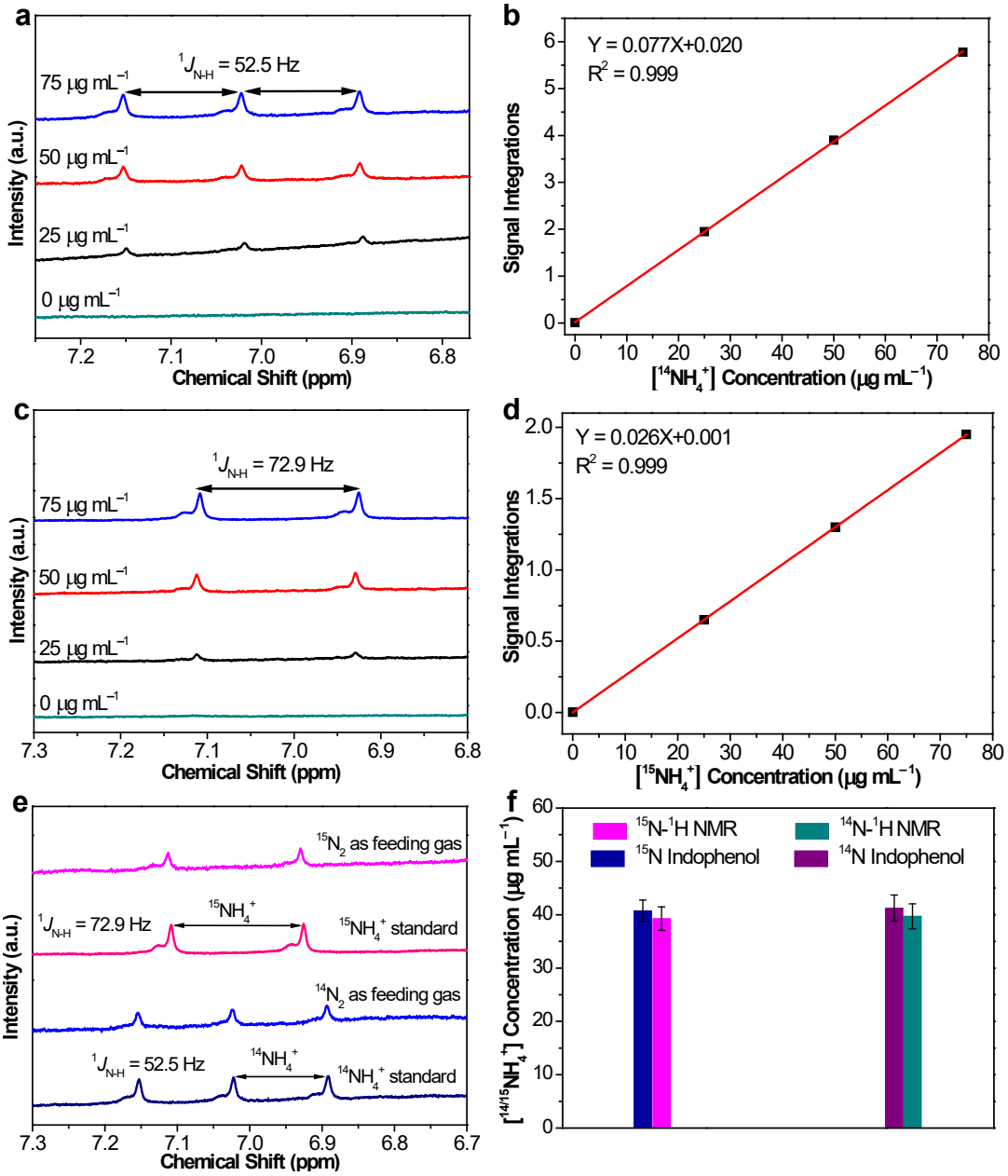

Supplementary Figure 18. (**a**) ^{1}H NMR spectra of $^{14}NH_4^+$ standards and (**b**) Corresponding $^{14}NH_4^+$ calibration curve. (**c**) ^{1}H NMR spectra of $^{15}NH_4^+$ standards and (**d**) Corresponding $^{15}NH_4^+$ calibration curve. (**e**) ^{1}H NMR spectra of $^{14}NH_4^+$ and $^{15}NH_4^+$ standards (75 μg mL^{-1}), and the resultant samples from Fe/Co-O-C-1.0 catalysed NRR using $^{14}N_2$ and $^{15}N_2$ feeding gases, respectively. (**f**) Yielded $^{14}NH_4^+$ and $^{15}NH_4^+$ concentrations in the resultant sample solutions determined by the indophenol blue and ^{1}H NMR methods. The error bars represents the data obtained from three replicated experiments.

The yielded $^{14}NH_4^+$ and $^{15}NH_4^+$ concentrations determined by ^{1}H NMR method are 39.7 ± 2.1 and 39.2 ± 2.4 μg mL^{-1}, corresponding to NH_3 yield rates of 535.7 ± 28.7 and 531.4 ± 32.8 μg h^{-1} $mg_{cat.}^{-1}$, respectively, very closely approximated to those determined by indophenol blue method (41.2 ± 2.8 μg mL^{-1} for $^{14}NH_4^+$ and 40.7 ± 2.6 μg mL^{-1} for $^{15}NH_4^+$, corresponding to NH_3 yield rates of 555.9 ± 37.8 and 551.4 ± 35.2 μg h^{-1} $mg_{cat.}^{-1}$, respectively).

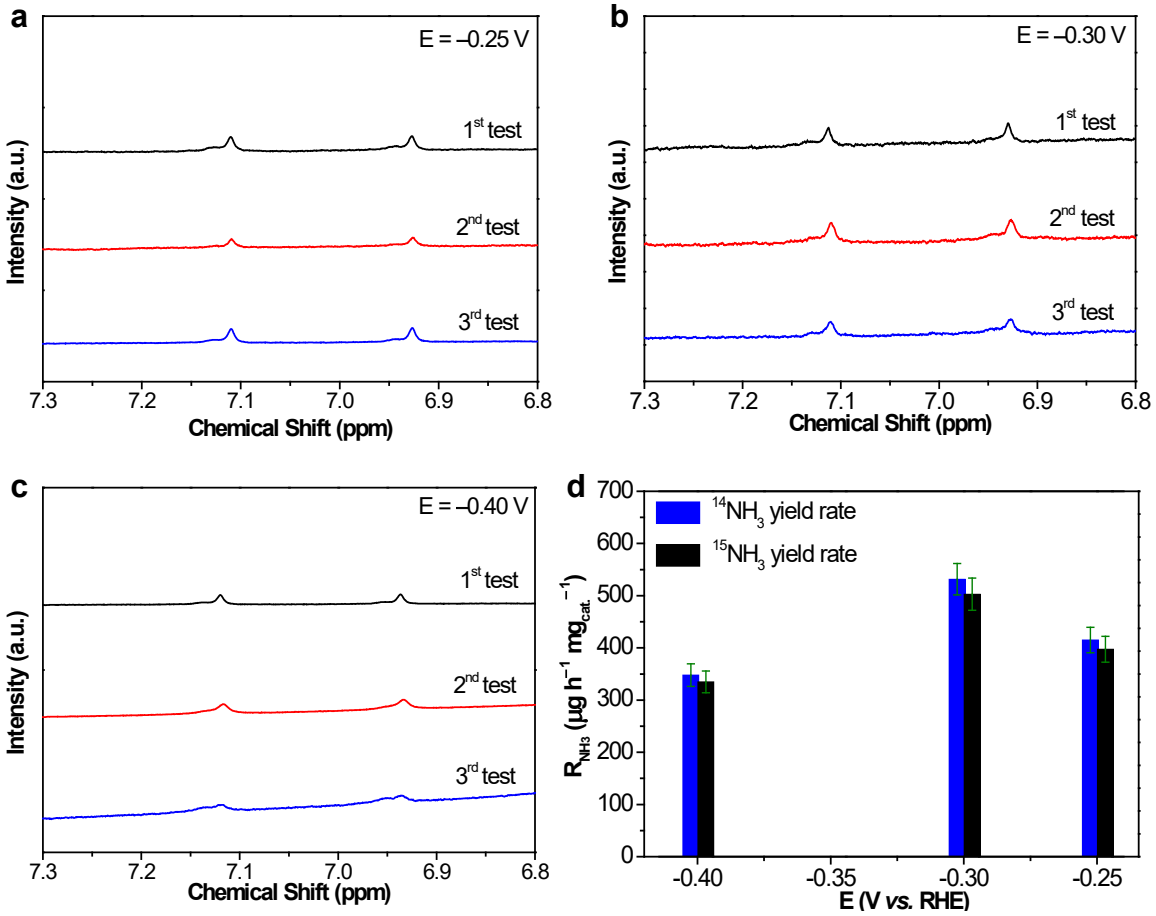

Supplementary Figure 19. ^{1}H NMR spectra of the yielded $^{15}NH_4^+$ by Fe/Co-O-C-1.0 electrode in 0.1 M Na_2SO_4 electrolyte for 2 h period with $^{15}N_2$ as feeding gas at different potentials of (**a**) −0.25 V, (**b**) −0.30 V and (**c**) −0.40 V (*vs.* RHE). (**d**) Comparison of NH_3 yield rates from Fe/Co-O-C-1.0 electrode using $^{14}N_2$ and $^{15}N_2$ as the feeding gases under different applied potentials. The yielded $^{15}NH_3$ was quantified by ^{1}H NMR analysis using the data derived from the ^{1}H NMR spectra shown in (**a**), (**b**) and (**c**). The yielded $^{14}NH_3$ determined by the indophenol blue method using the data derived from Fig. 3a in manuscript. The error bars represent data obtained from three replicated experiments.

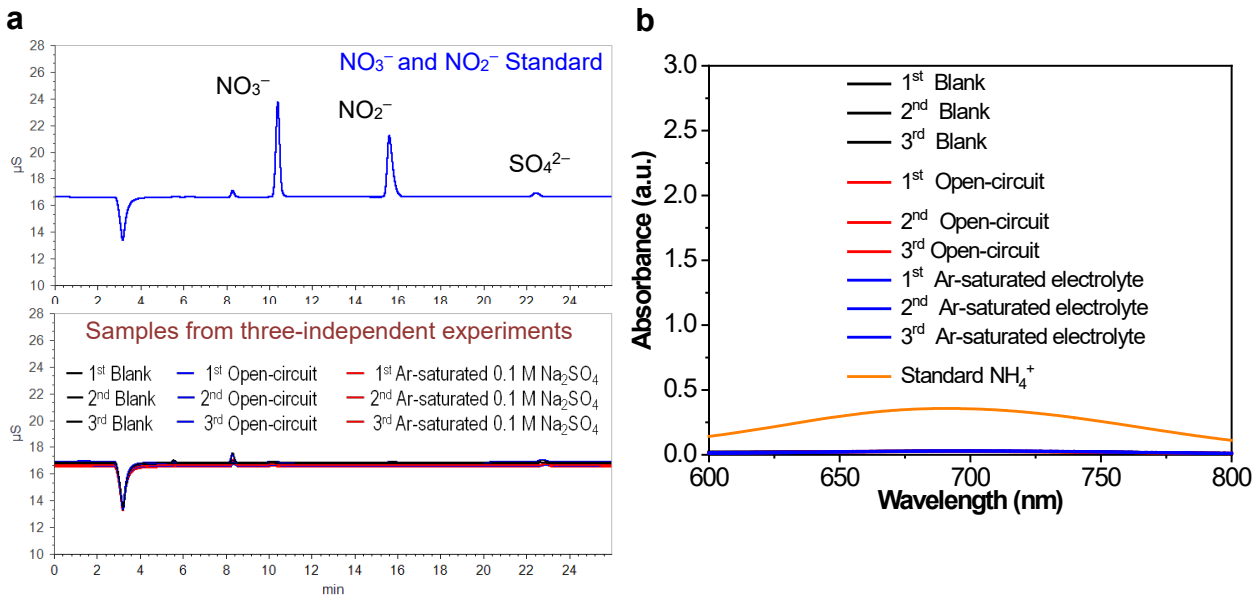

Supplementary Figure 20. (**a**) IC Chromatograms and **(b)** UV-Vis spectra of the standards, Blank (without Fe/Co-O-C-1.0 electrocatalyst but with −0.30 V *vs.* RHE in N_2-saturated 0.1 M Na_2SO_4 solution for 2 h), Open-circuit (with Fe/Co-O-C-1.0 electrocatalyst under open-circuit conditions in N_2-saturated 0.1 M Na_2SO_4 solution for 2 h) and Ar-saturated electrolyte (with Fe/Co-O-C-1.0 electrocatalyst under −0.30 V *vs.* RHE in Ar-saturated 0.1 M Na_2SO_4 solution for 2 h) samples from three independent experiments. IC Standard: 5.0 ppm of NO_3^- and NO_2^-. UV-Vis Standard: 0.50 ppm of NH_4^+. UV-Vis spectra were recorded from the treated samples in accordance with the indophenol blue method.

The above control experimental results unveiled that only ignorable NO_3^-, NO_2^- and NH_4^+ concentrations can be detected when the experiments were carried out using N_2- saturated 0.1 M Na_2SO_4 without electrocatalyst (blank), with electrocatalyst but without applied potential (open-circuit) and with electrocatalyst in Ar-saturated 0.1 M Na_2SO_4 at −0.30 V (*vs.* RHE) for 2 h. These control experimental results eliminate any noticeable environmental interference and further confirm that the yielded NH_3 is resulted exclusively from the Fe/Co-O-C-1.0 catalysed NRR.

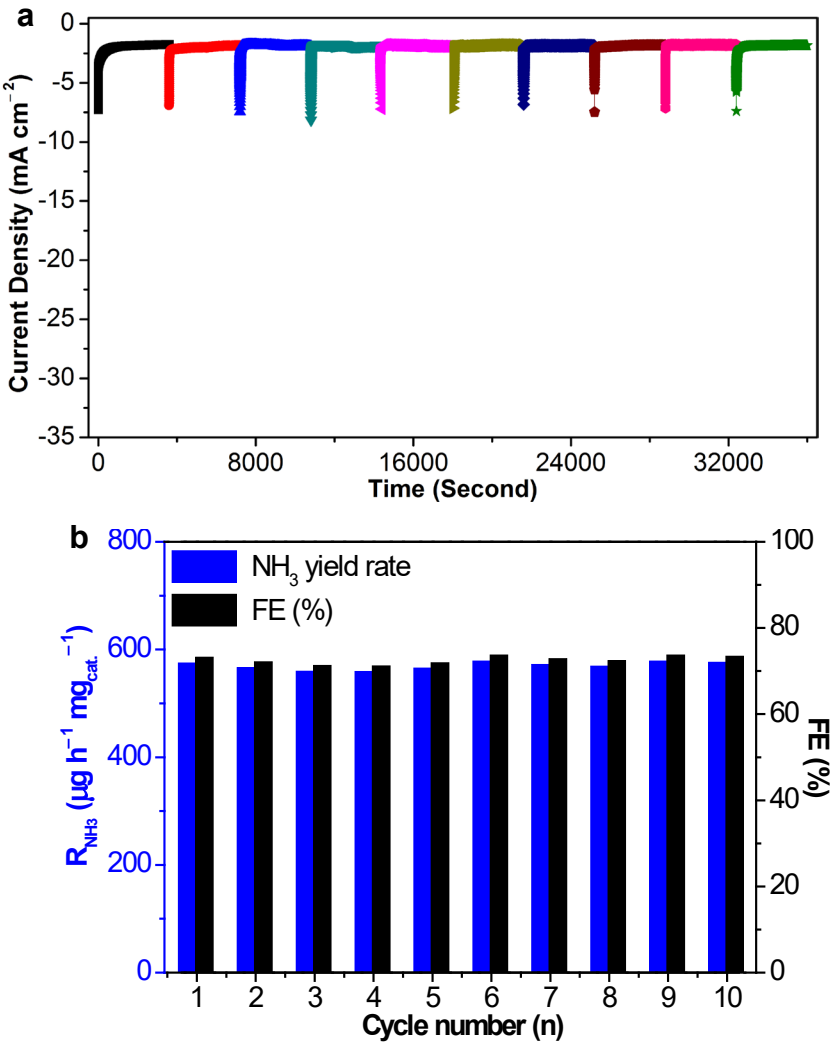

Supplementary Figure 21. (**a**) Cycling stability test of Fe/Co-O-C-1.0 in N_2-saturated 0.1 M Na_2SO_4 electrolyte at −0.30 V (*vs.* RHE) for 10 cycles with 1 h NRR period per cycle. (**b**) Corresponding R_{NH3} and FE derived from each testing cycle.

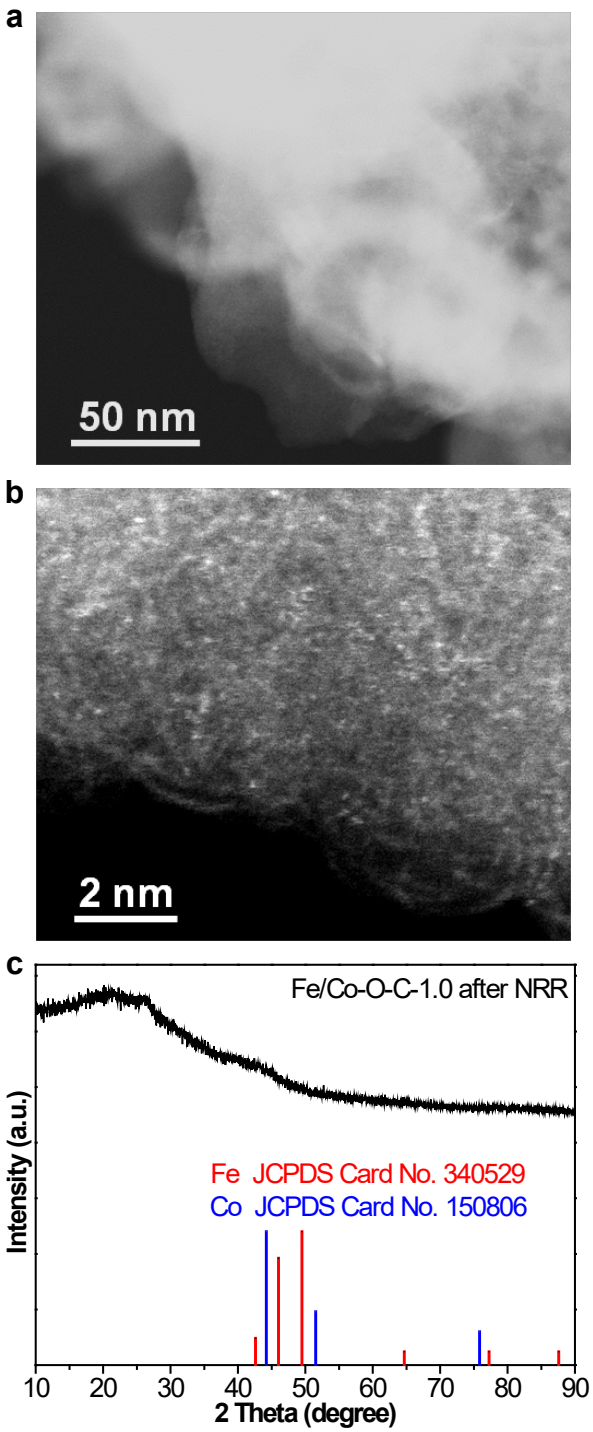

Supplementary Figure 22. (**a**) Low-, (**b**) High-magnification aberration-corrected HAADF-STEM images, and (**c**) XRD patterns of Fe/Co-O-C-1.0 after 72 h stability test.

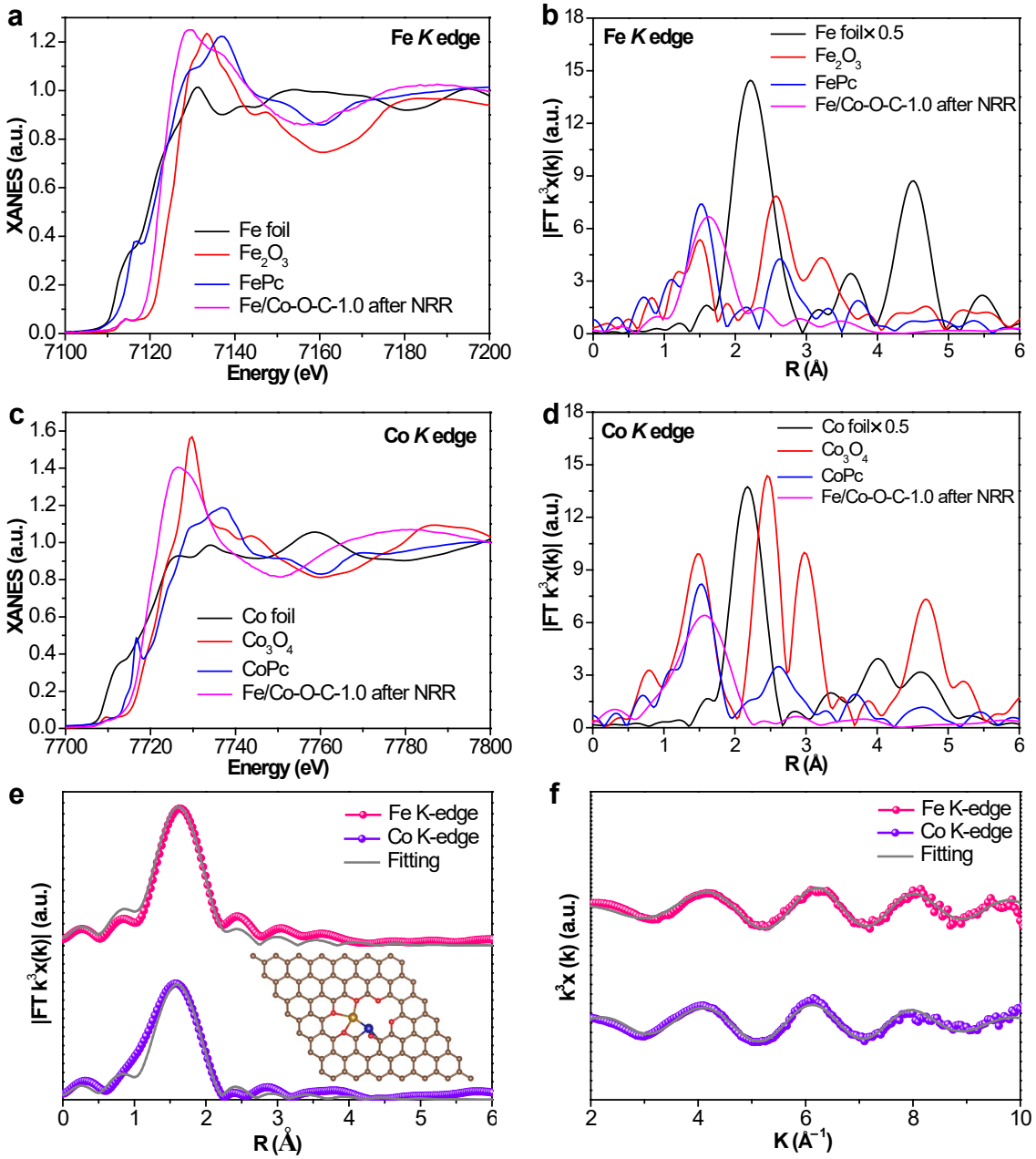

Supplementary Figure 23. Fe *K* edge (**a**) XANES spectra and (**b**) k^3-weighted FT-EXAFS spectra of Fe/Co-O-C-1.0 after 10 NRR cycles, and Fe foil (Noting that the spectrum is transformed by 0.5), Fe_2O_3. Co *K* edge (**c**) XANES spectra and (**d**) k^3-weighted FT-EXAFS spectra of Fe/Co-O-C-1.0 after 10 NRR cycles, Co foil (Noting that the spectrum is transformed by 0.5), Co_3O_4. (**e**, **f**) Fe *K* edge and Co *K* edge EXAFS fitting curves of $[(O\text{-}C_2)_3Fe\text{-}Co(O\text{-}C)C_2]$ configuration for Fe/Co-O-C-1.0 at *R* space and *k* space, respectively. Inset in (**e**) is the possible bimetallic Fe-Co coordination configurationin Fe/Co-O-C-1.0 after 10 NRR cycles (Brown: C, red: O, orange: Fe, blue: Co).

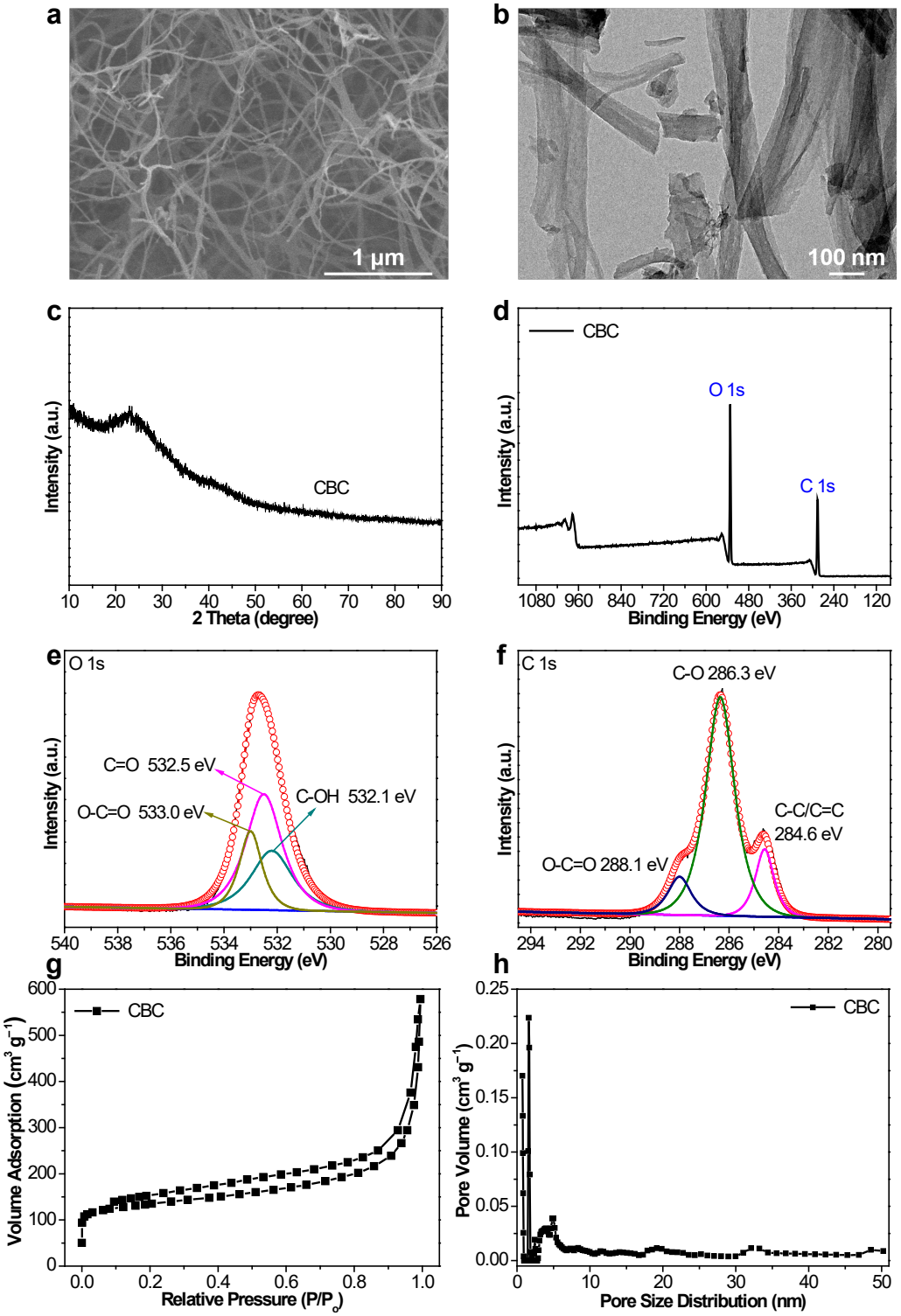

Supplementary Figure 24. (**a**) SEM image, (**b**) TEM image, (**c**) XRD pattern, (**d**) Survey XPS spectrum, (**e**) High-resolution O *1s* spectra, (**f**) High-resolution C *1s* spectra, (**g**) N_2 adsorption-desorption isotherm and (**h**) Corresponding pore size distribution curve of CBC.

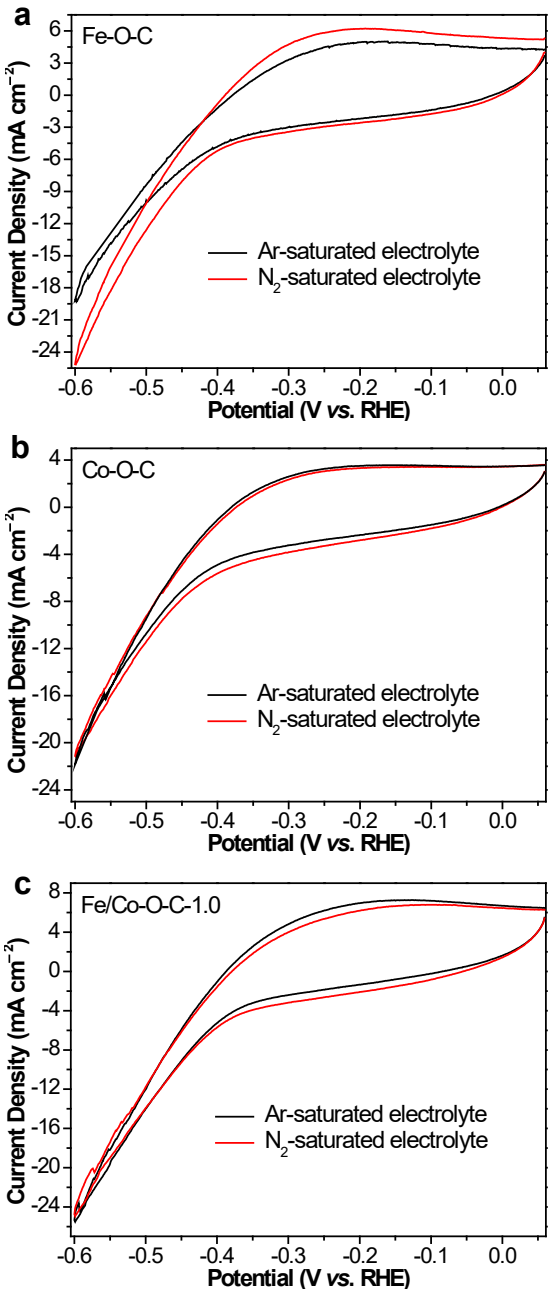

Supplementary Figure 25. CV curves of (**a**) Fe-O-C, (**b**) Co-O-C and (**c**) Fe/Co-O-C-1.0 in Ar- and N_2-saturated 0.1 M Na_2SO_4 electrolytes. Scan rate: 5.0 mV s^{-1}.

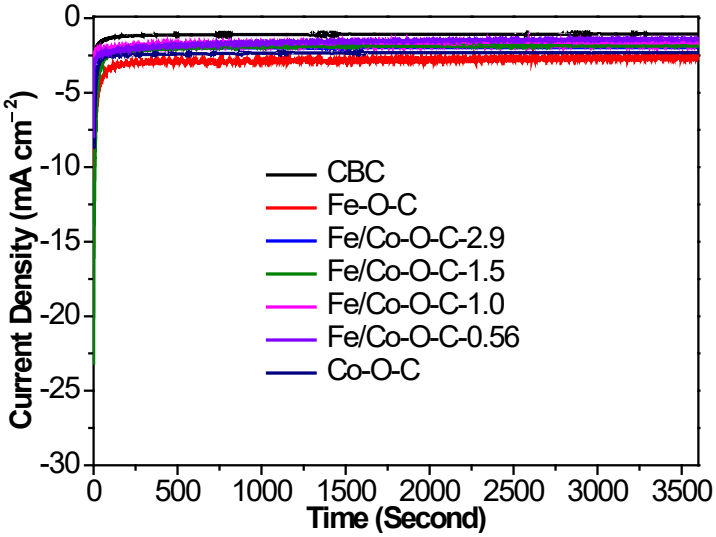

Supplementary Figure 26. Chronoamperometric responses of CBC, Fe-O-C, Fe/Co-O-C-2.9, Fe/Co-O-C-1.5, Fe/Co-O-C-1.0, Fe/Co-O-C-0.56 and Co-O-C catalysts at −0.30 V (*vs.* RHE) for 1 h reaction period in N_2-saturated 0.1 M Na_2SO_4 electrolyte.

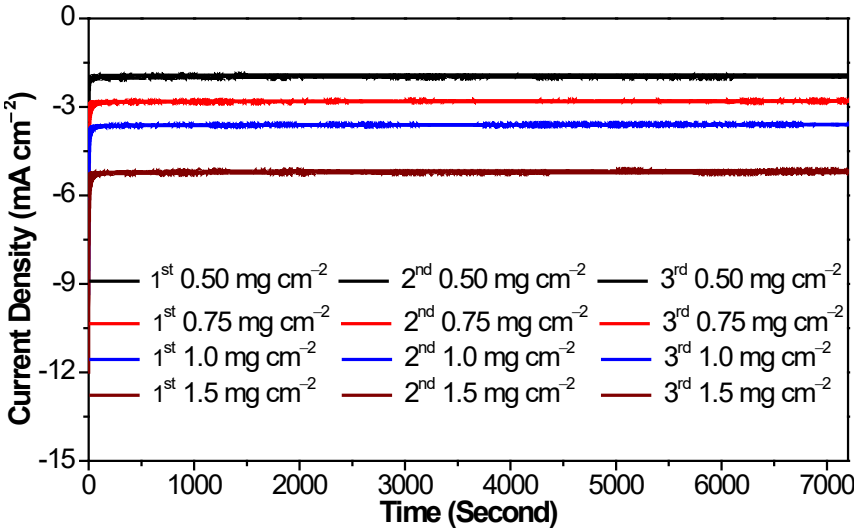

Supplementary Figure 27. Chronoamperometric curves of Fe/Co-O-C-1.0 with different loading amounts on GC plate electrode at −0.30 V *vs.* RHE.

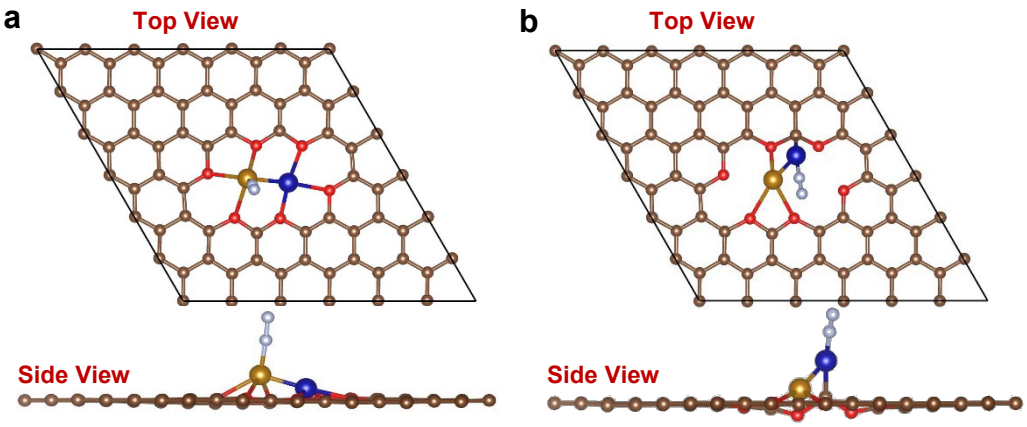

Supplementary Figure 28. DFT optimised end-on N_2 adsorption configurations on (**a**) Fe and (**b**) Co sites in $[(O\text{-}C_2)_3Fe\text{-}Co(O\text{-}C_2)_3]$.

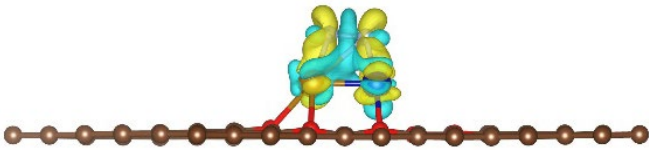

Supplementary Figure 29. DFT calculated Charge density differences ($\delta\rho=\rho A+B-\rho A-\rho B$) of side-on N_2 adsorption on $[(O\text{-}C_2)_3Fe\text{-}Co(O\text{-}C_2)_3]$. Yellow and cyan stand respectively for the electron accumulation and depletion. The isosurface value is 0.005 e/a_0^{-3}, where a_0 is the Bohr radius.

With the side-on adsorption, the calculated charge density difference discloses that the electrons in *d* orbitals of Fe and Co are transferred to the empty π* orbitals of N_2. As a result, the adsorbed N_2 gains 0.720 e^- from the bimetallic site, and the N-N bond is elongated from 1.120 Å (free gaseous N_2 state) to 1.225 Å, suggesting that the adsorbed N_2 is activated.

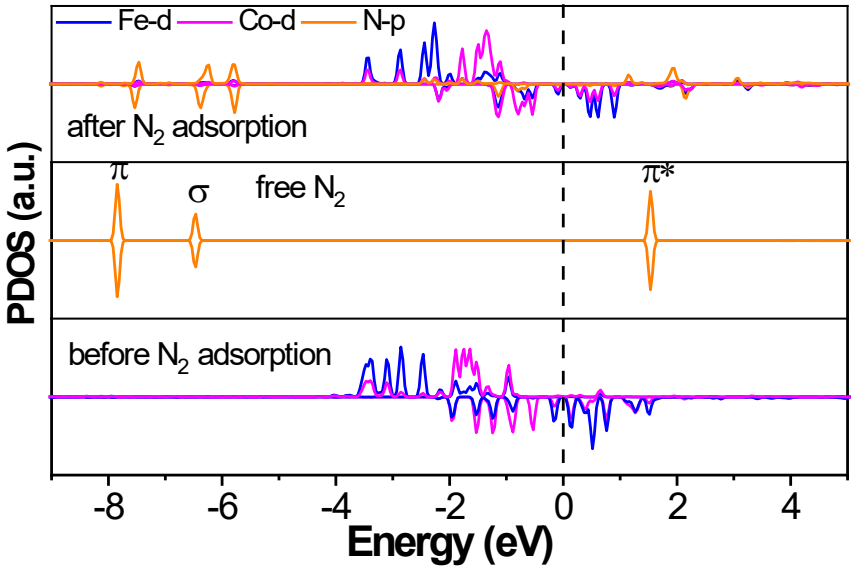

Supplementary Figure 30. Calculated PDOS for graphene with $[(O\text{-}C_2)_3Fe\text{-}Co(O\text{-}C_2)_3]$ before and after side-on N_2 adsorption.

The broadened Fe-3*d* and Co-3*d* states after N_2 adsorption addicting to the overlapped Fe, Co and N states imply the hybridized Fe/Co 3*d* orbitals with N 2*p* orbital. The overlapped PDOS between Fe-3*d* and $*N_2$-2*p*, and Co-3*d* and $*N_2$-2*p* are distributed below and above the Fermi energy, signifying a back-bonding between the bimetallic Fe-Co site and $*N_2$[69].

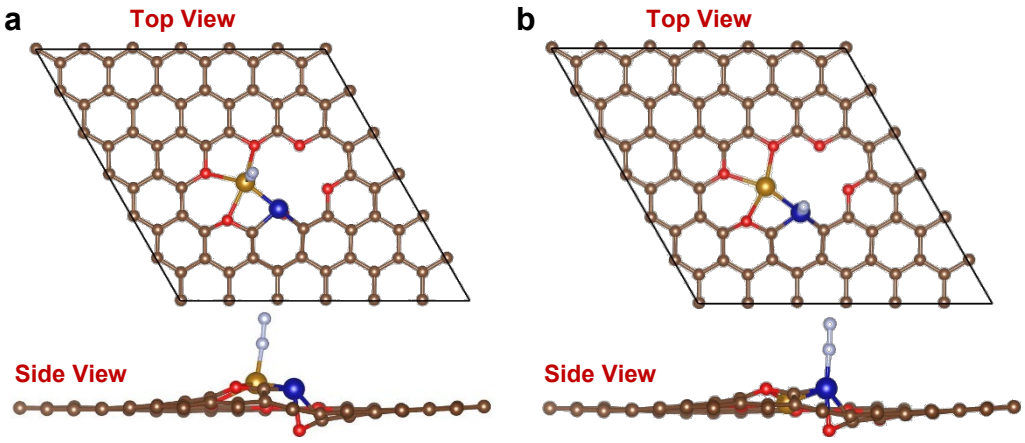

Supplementary Figure 31. DFT optimised end-on N_2 adsorption configurations on (**a**) Fe and (**b**) Co sites in $[(O\text{-}C_2)_3Fe\text{-}Co(O\text{-}C)C_2]$.

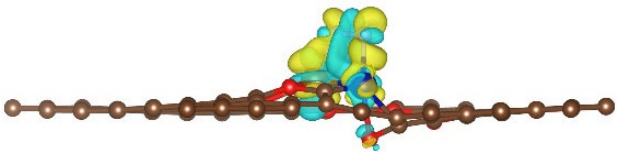

Supplementary Figure 32. DFT calculated Charge density differences ($\delta\rho=\rho A+B-\rho A-\rho B$) of side-on N_2 adsorption on [$(O\text{-}C_2)_3Fe\text{-}Co(O\text{-}C)C_2$]. Yellow and cyan stand respectively for the electron accumulation and depletion. The isosurface value is 0.005 e/a_0^{-3}, where a_0 is the Bohr radius.

The calculated charge density difference unveils that the side-on adsorbed N_2 gains 0.62 e^- from the Fe-Co site in [$(O\text{-}C_2)_3Fe\text{-}Co(O\text{-}C)C_2$].

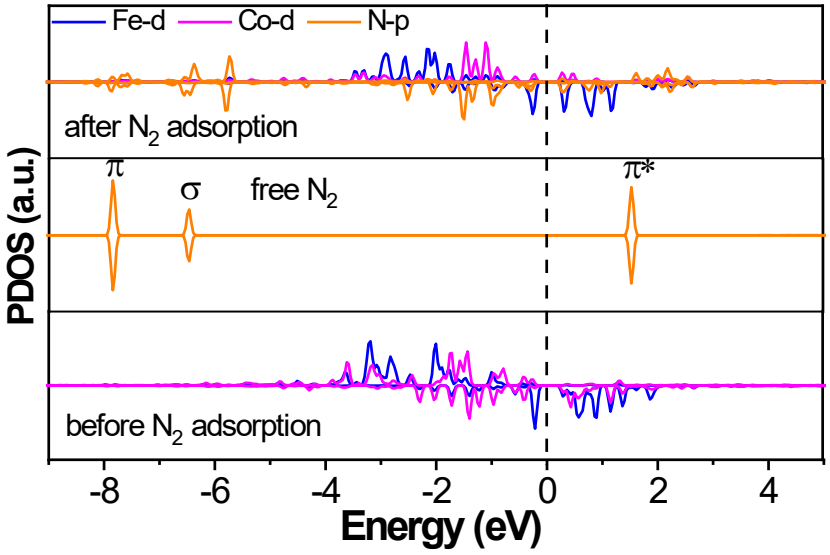

Supplementary Figure 33. Calculated PDOS for graphene with $[(O\text{-}C_2)_3Fe\text{-}Co(O\text{-}C)C_2]$ before and after side-on N_2 adsorption.

Deferring from $[(O\text{-}C_2)_3Fe\text{-}Co(O\text{-}C_2)_3]$, the PDOSs of $[(O\text{-}C_2)_3Fe\text{-}Co(O\text{-}C)C_2]$ uncover that the side-on adsorption on the Fe-Co site leads to the spin-down/beta orbital of Fe-3*d* being shifted away slightly from the Fermi level, suggesting a less effective charge transfer with $*N_2$.

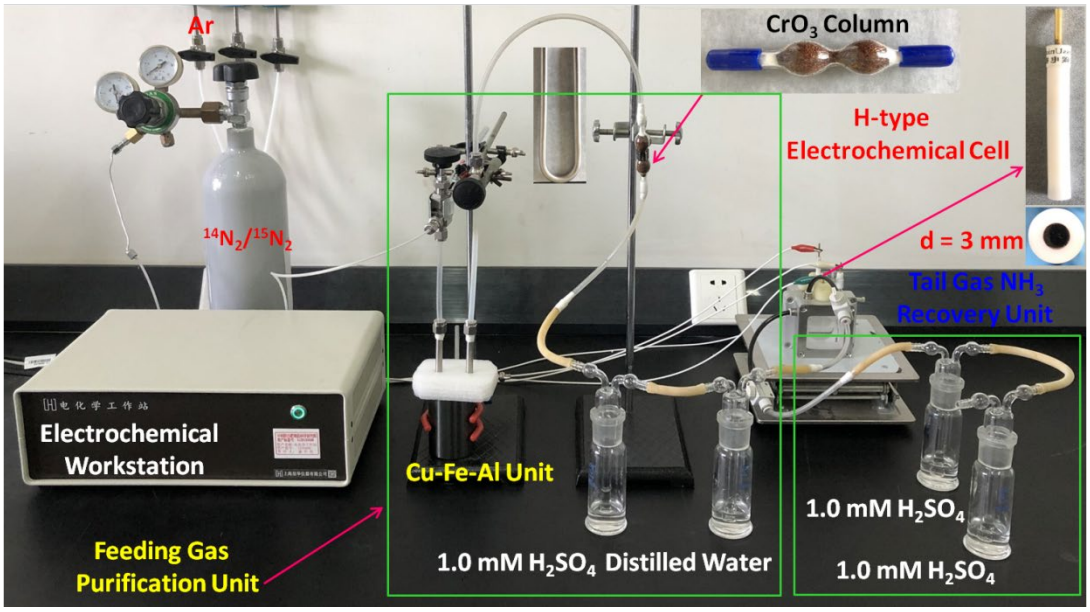

Supplementary Figure 34. Photograph of electrochemical experimental setup.

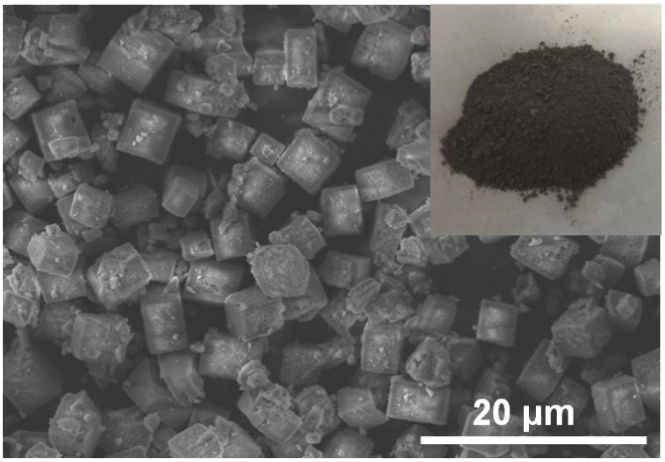

Supplementary Figure 35. SEM image and photograph (inset) of the synthesised Cu-Fe-Al catalyst.

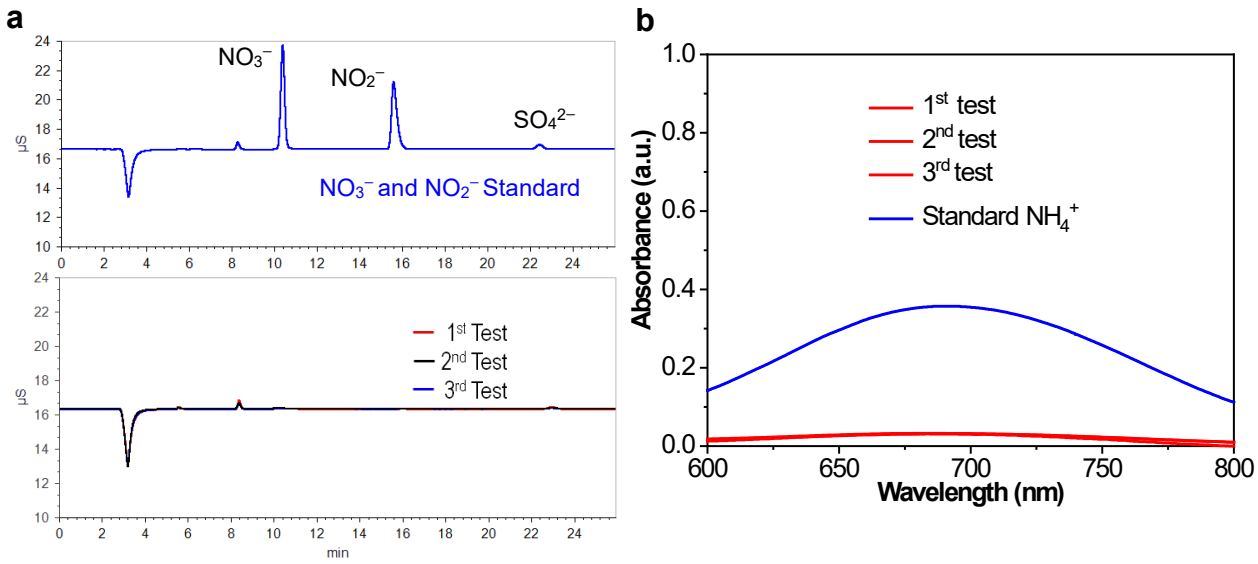

Supplementary Figure 36. (**a**) IC Chromatograms and **(b)** UV-Vis spectra of the standards and $^{14}N_2$ feeding gas samples from three replicated experiments. The experiments were carried by feeding $^{14}N_2$ at a flow rate of 20 mL min^{-1} through the purification unit into 30 mL of deionised water in the cathode chamber of the electrochemical cell for 1 h. IC Standard: 5.0 ppm of NO_3^- and NO_2^-. UV-Vis Standard: 0.50 ppm of NH_4^+. UV-Vis spectra were recorded from the treated samples in accordance with the indophenol blue method.

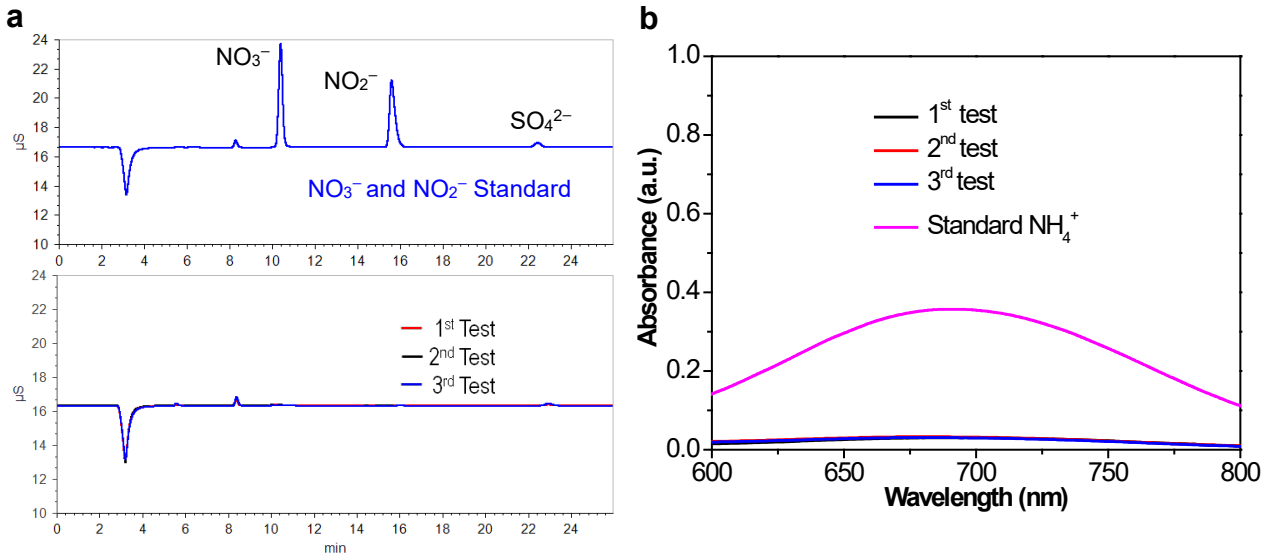

Supplementary Figure 37. (**a**) IC Chromatograms and **(b)** UV-Vis spectra of the standards and $^{15}N_2$ feeding gas samples from three replicated experiments. The experiments were carried by feeding $^{15}N_2$ at a flow rate of 20 mL min^{-1} through the purification unit into 30 mL of deionised water in the cathode chamber of the electrochemical cell for 1 h. IC Standard: 5.0 ppm of NO_3^- and NO_2^-. UV-Vis Standard: 0.50 ppm of NH_4^+. UV-Vis spectra were recorded from the treated samples in accordance with the indophenol blue method.

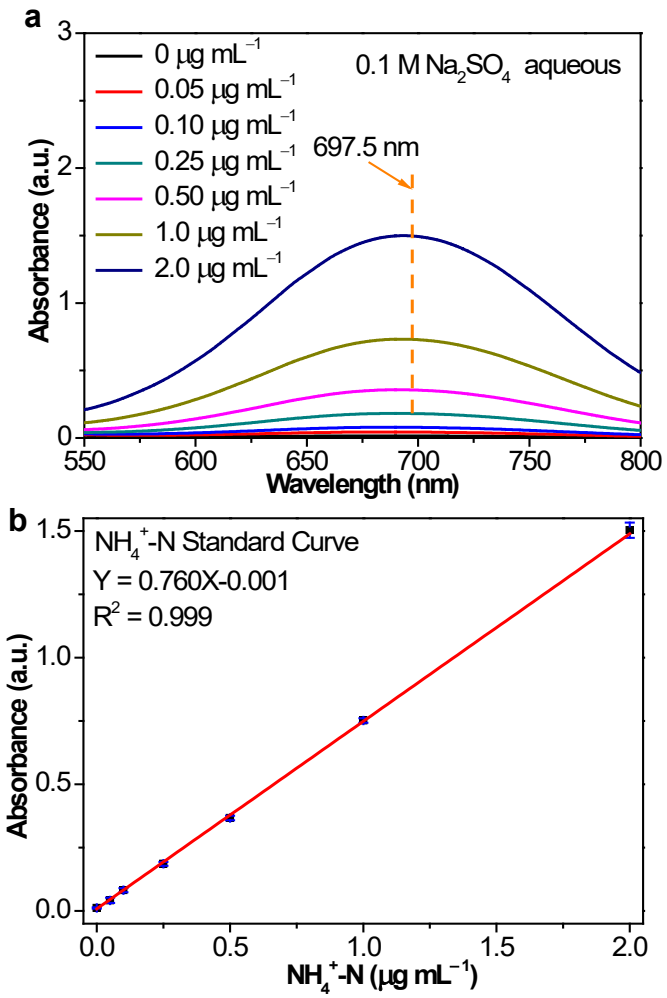

Supplementary Figure 38. (**a**) UV-Vis absorption spectra obtained from solutions with different NH_4^+-N concentrations (0, 0.05, 0.10, 0.25, 0.50, 1.0 and 2.0 μg mL^{-1}) incubated for 1 h at room temperature. (**b**) Calibration curve used to determine NH_4^+-N concentrations. The error bars represent data obtained from three replicated experiments.

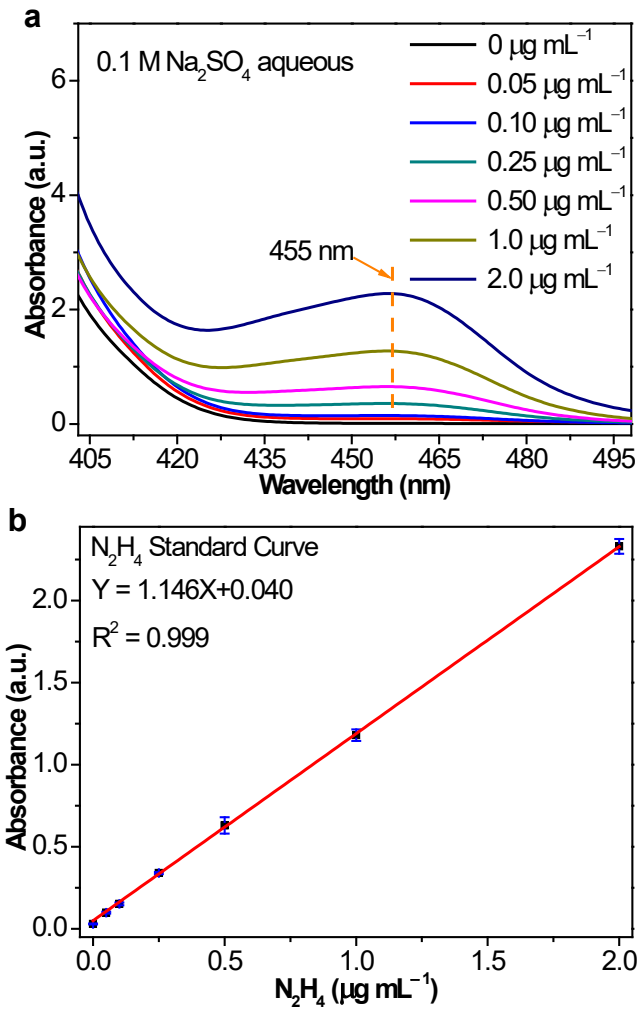

Supplementary Figure 39. (**a**) UV-Vis absorption spectra obtained from solutions with different N_2H_4 concentrations (0, 0.05, 0.10, 0.25, 0.50, 1.0 and 2.0 μg mL^{-1}) incubated for 20 min at room temperature. (**b**) Calibration curve used to determine N_2H_4 concentrations. The error bars represent data obtained from three replicated experiments.

Supplementary References

1. Wang, J., Yu, L., Hu, L., Chen, G., Xin, H. & Feng, X. Ambient ammonia synthesis via palladiumcatalyzed electrohydrogenation of dinitrogen at low overpotential. *Nat. Commun.* **9**, 1795−1801 (2018).
2. Shi, M-M., Bao, D., Wulan, B-R., Li, Y-H., Zhang, Y-F., Yan, J-M. & Jiang, Q. Au subnanoclusters on TiO_2 toward highly efficient and selective electrocatalyst for N_2 conversion to NH_3 at ambient conditions. *Adv. Mater.* **29**, 1606550 (2017).
3. Shi, M-M., Bao, D., Li, S-J., Wulan, B-R., Yan, J-M. & Jiang, Q. Anchoring PdCu amorphous nanocluster on graphene for electrochemical reduction of N_2 to NH_3 under ambient conditions in aqueous solution. *Adv. Energy Mater.* **8**, 1800124 (2018).
4. Huang, H., Xia, L., Shi, X., Asiri, AM. & Sun, X. Ag nanosheets for efficient electrocatalytic N_2 fixation to NH_3 under ambient conditions. *Chem. Commun.* **54**, 11427−11430 (2018).
5. Lee, HK. et al. Favoring the unfavored: selective electrochemical nitrogen fixation using a reticular chemistry approach. *Sci. Adv.* **4**, eaar3208 (2018).
6. Xue, Z-H. et al. Electrochemical reduction of N_2 into NH_3 by donor-acceptor couples of Ni and Au nanoparticles with a 67.8% faradaic efficiency. *J. Am. Chem. Soc.* **141**, 14976−14980 (2019).
7. Yang, C., Huang, B., Bai, S., Feng, Y., Shao, Q. & Huang, X. A generalized surface chalcogenation strategy for boosting the electrochemical N_2 fixation of metal nanocrystals. *Adv. Mater.* **32**, 2001267 (2020).
8. Xu, W. et al. Nanoporous palladium hydride for electrocatalytic N_2 reduction under ambient conditions. *Angew. Chem. Int. Ed.* **59**, 3511–3516 (2020).
9. Ahmed, MI. et al. Metal-sulfur linkages achieved by organic tethering of ruthenium nanocrystals for enhanced electrochemical nitrogen reduction. *Angew. Chem. Int. Ed.* **59**, 21465−21469 (2020).
10. Tan, Y. et al. Fabrication of an Au_{25}-cys-Mo electrocatalyst for efficient nitrogen reduction to ammonia under ambient conditions. *Small* **17**, 2100372 (2021).
11. Guo, Y. et al. Regulating nitrogenous adsorption and desorption on Pd clusters by the acetylene linkages of hydrogen substituted graphdiyne for efficient electrocatalytic ammonia synthesis. *Nano Energy* **86**, 106099 (2021).
12. Zhao, C. et al. Ambient electrosynthesis of ammonia on a biomass-derived nitrogen-doped porous carbon electrocatalyst: contribution of pyridinic nitrogen. *ACS Energy Lett.* **4**, 377−383 (2019).
13. Qiu, W. et al. High-performance artificial nitrogen fixation at ambient conditions using a metal-free electrocatalyst. *Nat. Commun.* **9**, 3485 (2018).
14. Yuan, D. et al. Electron distribution tuning of fluorine-doped carbon for ammonia electrosynthesis. *J. Mater. Chem. A* **7**, 16979−16983 (2019).
15. Zhu, X. et al. Ambient electrohydrogenation of N_2 for NH_3 synthesis on non-metal boron phosphide nanoparticles: the critical role of P in boosting the catalytic activity. *J. Mater. Chem. A* **7**, 16117−16121 (2019).
16. Zhang, X. et al. Boron nanosheet: an elemental two-dimensional (2D) material for ambient electrocatalytic N_2-to-NH_3 fixation in neutral media. *ACS Catal.* **9**, 4609−4615 (2019).
17. Liu, S., Wang, M., Qian, T., Ji, H., Liu, J. & Yan, C. Facilitating nitrogen accessibility to boron-rich covalent organic frameworks via electrochemical excitation for efficient nitrogen fixation. *Nat. Commun.* **10**, 3898 (2019).
18. McPherson, IJ., Sudmeier, T., Fellowes, JP., Wilkinson, I., Hughes, T. & Tsang, ESC. The feasibility of electrochemical ammonia synthesis in molten LiCl-KCl eutectics. *Angew. Chem. Int. Ed.* **58**, 17433−17441 (2019).

19. Liu, Y. et al. A highly efficient metal-free electrocatalyst of F-doped porous carbon toward N_2 electroreduction. *Adv. Mater.* **32**, 1907690 (2020).
20. Liu, B. et al. Nanostructured and boron-doped diamond as an electrocatalyst for nitrogen fixation. *ACS Energy Lett.* **5**, 2590−2596 (2020).
21. Liu, Q. et al. Crystalline red phosphorus nanoribbons: large-scale synthesis and electrochemical nitrogen fixation. *Angew. Chem. Int. Ed.* **59**, 14383−14387 (2020).
22. Lin, Y-X. et al. Boosting selective nitrogen reduction to ammonia on electron-deficient copper nanoparticles. *Nat. Commun.* **10**, 4380 (2019).
23. Liu, Y-T., Tang, L., Dai, J., Yu, J. & Ding, B. Promoted electrocatalytic nitrogen fixation in Fe-Ni layered double hydroxide arrays coupled to carbon nanofibers: the role of phosphorus doping. *Angew. Chem. Int. Ed.* **59**, 13623−13627 (2020).
24. Wang, H-B. et al. Bionic design of a Mo(IV)-doped FeS_2 catalyst for electroreduction of dinitrogen to ammonia. *ACS Catal.* **10**, 4914−4921 (2020).
25. Fang, Y. et al. Graphdiyne interface engineering: highly active and selective ammonia synthesis. *Angew. Chem. Int. Ed.* **59**, 13021−13027 (2020).
26. Tong, Y. et al. Vacancy engineering of iron-doped $W_{18}O_{49}$ nanoreactors for low-barrier electrochemical nitrogen reduction. *Angew. Chem. Int. Ed.* **59**, 7356−7361 (2020).
27. Lai, F. et al. Refining energy levels in ReS_2 nanosheets by low-valent transition-metal doping for dual-boosted electrochemical ammonia/hydrogen production. *Adv. Funct. Mater.* **30**, 1907376 (2020).
28. Liu, S., Wang, M., Ji, H., Shen, X., Yan, C. & Qian, T. Altering the rate-determining step over cobalt single clusters leading to highly efficient ammonia synthesis. *Natl. Sci. Rev.* **8**, nwaa136 (2021).
29. Ba, K. et al. Single faceted two-dimensional Mo_2C electrocatalyst for highly efficient nitrogen fixation. *ACS Catal.* **10**, 7864−7870 (2020).
30. Lv, X-W., Liu, X-L., Suo, Y-J., Liu, Y-P. & Yuan, Z-Y. Identifying the dominant role of pyridinic-N-Mo bonding in synergistic electrocatalysis for ambient nitrogen reduction. *ACS Nano* **15**, 12109−12118 (2021).
31. Zhao, Y. et al. Identification of M-NH_2-NH_2 intermediate and rate determining step for nitrogen reduction with bioinspired sulfur-bonded FeW catalyst. *Angew. Chem. Int. Ed.* **60**, 20331−20341 (2021).
32. Chen, J. et al. The activation of porous atomic layered MoS_2 basal-plane to induce adjacent Mo atom pairs promoting high efficiency electrochemical N_2 fixation. *Appl. Catal. B: Environ.* **285**, 119810 (2021).
33. Liao, W. et al. Interfacial engineering promoting electrosynthesis of ammonia over Mo/phosphotungstic acid with high performance. *Adv. Funct. Mater.* **31**, 2009151 (2021).
34. Liu, X. et al. Antimony-based composites loaded on phosphorus-doped carbon for boosting faradaic efficiency of the electrochemical nitrogen reduction reaction. *Angew. Chem. Int. Ed.* **58**, 13329−13334 (2019).
35. Liu, Y-T., Li, D., Yu, J. & Ding, B. Stable confinement of black phosphorus quantum dots on black tin oxide nanotubes: a robust, double-active electrocatalyst toward efficient nitrogen fixation. *Angew. Chem. Int. Ed.* **131**, 16591−16595 (2019).
36. Li, L., Tang, C., Xia, B., Jin, H., Zheng, Y. & Qiao, S-Z. Two-dimensional mosaic bismuth nanosheets for highly selective ambient electrocatalytic nitrogen reduction. *ACS Catal.* **9**, 2902−2908 (2019).
37. Hao, Y-C. et al. Promoting nitrogen electroreduction to ammonia with bismuth nanocrystals and potassium cations in water. *Nat. Catal.* **2**, 448−456 (2019).
38. Wang, Y. et al. Generating defect-rich bismuth for enhancing the rate of nitrogen electroreduction to ammonia. *Angew Chem Int Ed.* **58**, 9464−9469 (2019).

39. Zhang, R. et al. Electrocatalytic N_2-to-NH_3 conversion with high faradaic efficiency enabled using a Bi nanosheet array. *Chem. Commun.* **55**, 5263−5266 (2019).
40. Guo, Y. et al. A rechargeable Al-N_2 battery for energy storage and highly efficient N_2 fixation. *Energy Environ.Sci.* **13**, 2888−2895 (2020).
41. Yao, D. et al. In situ fragmented bismuth nanoparticles for electrocatalytic nitrogen reduction. *Adv. Energy Mater.* **10**, 2001289 (2020).
42. Wan, Y. et al. Oxidation state modulation of bismuth for efficient electrocatalytic nitrogen reduction to ammonia. *Adv. Funct. Mater.* **31**, 2100300 (2021).
43. Wang, X. et al. Atomically dispersed Au_1 catalyst towards efficient electrochemical synthesis of ammonia. *Sci. Bull.* **63**, 1246−1253 (2018).
44. Geng, Z. et al. Achieving a record-high yield rate of 120.9 for N_2 electrochemical reduction over Ru single-atom catalysts. *Adv. Mater.* **30**, 1803498 (2018).
45. Tao, H. et al. Nitrogen fixation by Ru single-atom electrocatalytic reduction. *Chem* **5**, 204−214 (2019).
46. Han, L. et al. Atomically dispersed molybdenum catalysts for efficient ambient nitrogen fixation. *Angew. Chem. Int. Ed.* **131**, 2343−2347 (2019).
47. Wang, M. et al. Over 56.55% Faradaic efficiency of ambient ammonia synthesis enabled by positively shifting the reaction potential. *Nat. Commun.* **10**, 341 (2019).
48. Lü, F. et al. Nitrogen-coordinated single Fe sites for efficient electrocatalytic N_2 fixation in neutral media. *Nano Energy* **61**, 420−427 (2019).
49. Hui, L. et al. Highly efficient and selective generation of ammonia and hydrogen on a graphdiyne-based catalyst. *J. Am. Chem. Soc.* **141**, 10677−10683 (2019).
50. Zang, W. et al. Copper single atoms anchored in porous nitrogen-doped carbon as efficient pH-universal catalysts for the nitrogen reduction reaction. *ACS Catal.* **9**, 10166−10173 (2019).
51. Zhang, R., Jiao, L., Yang, W., Wan, G. & Jiang, H-L. Single-atom catalysts templated by metal-organic frameworks for electrochemical nitrogen reduction. *J. Mater. Chem. A* **7**, 26371−26377 (2019).
52. Liu, Y. et al. Electrochemical reduction of N_2 to ammonia on Co single atom embedded N-doped porous carbon under ambient conditions. *J. Mater. Chem. A* **7**, 26358−26363 (2019).
53. Yu, B. et al. Tuning the catalytic preference of ruthenium catalysts for nitrogen reduction by atomic dispersion. *Adv. Funct. Mater.* **30**, 1905665 (2020).
54. Zhang, S. et al. Electrocatalytically active Fe-$(O\text{-}C_2)_4$ single-atom sites for efficient reduction of nitrogen to ammonia. *Angew. Chem. Int. Ed.* **59**, 13423−13429 (2020).
55. Zhang, S. et al. Laser irradiation in liquid to release cobalt single-atom sites for efficient electrocatalytic N_2 reduction. *ACS Appl. Energy Mater.* **3**, 6079−6086 (2020).
56. Zhang, L. et al. A janus Fe-SnO_2 catalyst that enables bifunctional electrochemical nitrogen fixation. *Angew. Chem. Int. Ed.* **59**, 10888−10893 (2020).
57. Peng, W. et al. Spontaneous atomic ruthenium doping in Mo_2CT_X MXene defects enhances Electrocatalytic activity for the nitrogen reduction reaction. *Adv. Energy Mater.* **10**, 2001364 (2020).
58. Li, J. et al. Accelerated dinitrogen electroreduction to ammonia via interfacial polarization triggered by single-atom protrusions. *Chem* **6**, 885−901 (2020).
59. Ma, Y. et al. Synergizing Mo single atoms and Mo_2C nanoparticles on CNTs synchronizes selectivity and activity of electrocatalytic N_2 reduction to ammonia. *Adv. Mater.* **32**, 2002177 (2020).
60. Su, H. et al. Single atoms of iron on MoS_2 nanosheets for N_2 electroreduction into ammonia. *Angew. Chem. Int. Ed.* **59**, 20411−20416 (2020).

61. Chen, Y. et al. Highly productive electrosynthesis of ammonia by admolecule-targeting single Ag sites. *ACS Nano* **14**, 6938−6946 (2020).
62. Yu, H. et al. Graphdiyne based metal atomic catalysts for synthesizing ammonia. *Natl. Sci. Rev.* **8**, nwaa213 (2021).
63. Han, L. et al. Local modulation of single-atomic Mn sites for enhanced ambient ammonia electrosynthesis. *ACS Catal.* **11**, 509−516 (2021).
64. Mukherjee, S. et al. Atomically dispersed single Ni site catalysts for nitrogen reduction toward electrochemical ammonia synthesis using N_2 and H_2O. *Small Methods* **4**, 1900821 (2020).
65. Liu, J., Kong, X., Zheng, L., Guo, X., Liu, X. & Shui, J. Rare earth single-atom catalysts for nitrogen and carbon dioxide reduction. *ACS Nano* **14**, 1093−1101 (2020).
66. Wang, X. et al. Confined Fe-Cu clusters as sub-nanometer reactors for efficiently regulating the electrochemical nitrogen reduction reaction. *Adv. Mater.* **32**, 2004382 (2020).
67. Han, L. et al. Modulating single-atom palladium sites with copper for enhanced ambient ammonia electrosynthesis. *Angew. Chem. Int. Ed.* **60**, 345−350 (2021).
68. Lu, Z. et al. An isolated zinc-cobalt atomic pair for highly active and durable oxygen reduction. *Angew. Chem. Int. Ed.* **58**, 2622−2626 (2019).
69. Tong, Rice, C., Wieckowski, A. & Oldfield, E. A detailed NMR-based model for CO on Pt catalysts in an electrochemical environment: shifts, relaxation, back-bonding, and the Fermi-level local density of states. *J. Am. Chem. Soc.* **122**, 1123−1129 (2000).